

In-situ Rb-Sr geochronology of white mica in young metamafic and metasomatic rocks from Syros: testing the limits of LA-ICP-MS/MS mica dating using different anchoring approaches

Jesús Muñoz-Montecinos¹, Andrea Giuliani^{2,3}, Senan Oesch², Silvia Volante¹, Bradley Peters², Whitney Behr¹

¹ Institute of Geology, Department of Earth and Planetary Sciences, ETH Zurich, Sonneggstrasse 5, 8092, Zurich, Switzerland.

² Institute of Geochemistry and Petrology, Department of Earth Sciences, ETH Zurich, Clausiusstrasse 25, Zurich, 8092, Switzerland.

³ Earth and Planets Laboratory, Carnegie Institution for Science, 5241 Broad Branch Rd NW, Washington, 20015 DC, United States.

* Correspondence to: Jesús Muñoz-Montecinos (jmunoz@ethz.ch)

Abstract

The recent development of LA-ICP-MS/MS has revolutionized Rb-Sr mica dating allowing to obtain isotopic data within their microstructural context. While effective for old and felsic materials, this method presents challenges for young metamafic and metasomatic rocks due to limited radiogenic ingrowth associated with low Rb/Sr and young ages. We quantitatively address these limitations by combining laser ablation ICP-MS/MS and MC-ICP-MS data for coexisting white mica and epidote, respectively, for 10 Cenozoic metamorphic rocks from Syros Island (Greece). White mica analyses from metamafic and metasomatic rocks yield limited Rb/Sr spread, which typically does not exceed one order of magnitude ($^{87}\text{Rb}/^{86}\text{Sr} = 14$ to 231 for the combined dataset), and low radiogenic $^{87}\text{Sr}/^{86}\text{Sr}$ (generally <0.8), resulting in high age uncertainties of typically 10 to 50% relative standard error (RSE), and thus hampering robust geological interpretations. Epidote $^{87}\text{Sr}/^{86}\text{Sr}$ values range between ~ 0.705 and 0.708 . The former is typically expected for unaltered metamafic materials, whereas the latter is interpreted to reflect fluid-rock interaction along shear zones, with fluids derived from or having interacted with more radiogenic lithologies. These atypical values suggest that a commonly assumed value of 0.703 for mafic rocks may not always be representative. Anchoring white mica Rb-Sr to epidote $^{87}\text{Sr}/^{86}\text{Sr}$ data improves age accuracy and precision substantially (e.g., 29 ± 17 Ma vs 47.2 ± 4.4 Ma for sample SYGR36). The new ages obtained in this study are consistent with multiple events previously recorded in Syros and the Cyclades blueschists unit including: i) metasomatism and metamorphism at near-peak to epidote blueschist-facies conditions during early exhumation (c. 47 Ma to 41 Ma); and ii) a late stage of high-pressure exhumation and metasomatism transitioning to blueschist-greenschist facies conditions (c. 21 Ma to 20 Ma). Anchored white-mica Rb-Sr ages in mafic rocks allow us to discriminate events of fluid-rock interactions and metasomatism associated with shear zone deformation at the subduction interface.

Keywords

Rb-Sr dating; White mica; epidote; Syros; Metamorphism; Metasomatism

45 Introduction

46 Subduction zones host a wide range of mechanical and chemical processes that occur at various
47 spatial and temporal scales including seismicity, element transfer, volcanism and orogenesis
48 (e.g., Breeding et al., 2004; Burg and Bouilhol, 2019; Muñoz-Montecinos et al., 2021; Li et al.
49 2021; Wirth et al., 2022; Tumiati et al., 2022; Bastias et al., 2023; Rubatto et al., 2023). These
50 processes are temporally associated with metamorphism, fluid-rock interactions and
51 metasomatism at depth and occur over time-scales ranging from those of steady-state tectonics
52 (e.g., nappe stacking over millions of years; Rubatto et al., 2011; Holtmann et al., 2022) to
53 nearly instantaneous mineral growth and fluid flow (John et al., 2012). Constraining the timing
54 of high-pressure and low-temperature (HP-LT) mineral growth and fabric development is
55 therefore crucial for understanding deep tectono-thermal processes. However, accurately
56 dating these subduction-related metamorphic events remains challenging.

57
58 Compared to felsic rocks, dating metamafic rocks is challenging due to the paucity of minerals
59 amenable to geochronology. While the U-Pb system has been employed to date HP-LT mafic
60 metamorphic rocks, it relies on the presence of U-bearing accessory phases such as zircon,
61 allanite, titanite, rutile, and apatite which may be scarce, too small to be targeted, or have low-
62 U concentrations (e.g., Timmermann et al., 2004; Rubatto et al., 2011; Regis et al., 2014; Engi
63 et al. 2017; Holtmann et al., 2022; Volante et al. 2024 and references therein). Additionally, it
64 is challenging to link microstructures with U-Pb dates of accessory minerals due to their often-
65 ambiguous textural association with the microfabrics. Therefore, alternative minerals and
66 systematics are essential for a comprehensive record of deformation and metamorphism in HP
67 metamafic rocks.

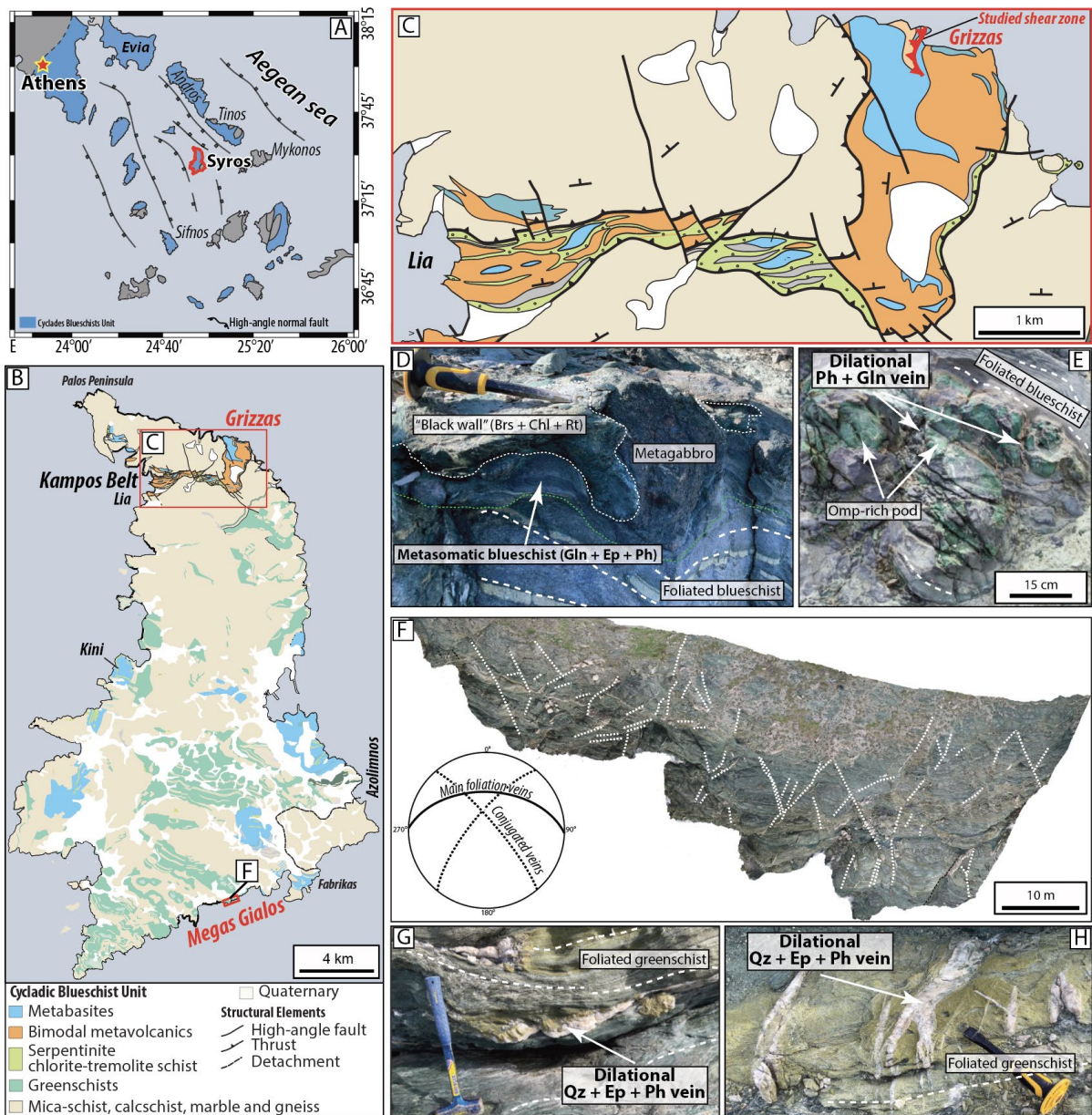
68
69 White mica is a common mineral in HP-LT altered oceanic metamafic and metasedimentary
70 lithologies and is stable throughout prograde and retrograde reactions (Schmidt et al., 2004;
71 Halama et al., 2020). The high Rb contents and the estimated high closure temperature of the
72 Rb-Sr system in this mineral (500 ± 50 °C – Jäger et al., 1967; von Blanckenburg et al, 1989;
73 Villa, 1998; Glodny et al. 1998, 2008) make white mica a suitable geochronometer for dating
74 subduction-related processes, especially when combined with low Rb/Sr phases. Despite the
75 robustness of multimineral Rb-Sr isochron analyses (Glodny et al., 2004, 2008; Wawrzenitz et
76 al., 2006; Bröcker et al., 2013; Kirchner et al., 2016; Angiboust and Glodny, 2020), significant
77 challenges remain. These include: i) Sr isotope disequilibrium between micas and the other
78 mineral phases; ii) coexistence of several generations of micas; iii) post-deformation, low-
79 temperature magmatic alteration or fluid-assisted recrystallization; iv) thermally-induced
80 diffusion processes (Glodny and Ring 2022); and v) potential inheritance within mica grains
81 or across mica populations (Villa, 2016; Barnes et al., 2024). These variations in mica Rb-Sr
82 systematics and isotopic variability can be directly addressed using in-situ laser ablation
83 methods (e.g., Ribeiro et al., 2023a).

84
85 In-situ Rb-Sr dating of white mica using a laser-ablation triple-quadrupole inductively coupled
86 plasma mass spectrometer (LA-ICP-MS/MS) offers significant advantages over conventional

87 ID (isotope dilution) TIMS analyses. This technique eliminates the need for mineral separation
88 and time-consuming chromatographic column chemistry, enabling quick, cost-effective
89 analyses. It further allows to constrain potential zoning in Rb-Sr isotope distribution
90 (Kutzschbach and Glodny, 2024; Rösel and Zack, 2021), hence preserving essential textural
91 information which is otherwise lost. Thus, potential age variations among different white mica
92 populations (e.g., syn- to post-kinematic grains) within distinct microstructural domains such
93 as microfolds, shear zones, and boudin necks permit a more accurate interpretation of the
94 resulting ages (Gou et al., 2022; Gyomlai et al., 2022, 2023a; Kirkland et al., 2023; Ribeiro et
95 al., 2023b; Ceccato et al., 2024; Barnes et al., 2024). This method has been extensively applied
96 to constrain the timing of deformation events in Precambrian-Paleozoic felsic lithologies
97 (Olierook et al., 2020; Tillberg et al., 2021; Wang et al., 2022; Ribeiro et al., 2023b), but its
98 application remains limited in mafic lithologies. For example, a recent study on mafic
99 blueschist from the Syros island (Greece) presented white mica-only isochron ages interpreted
100 to date fluid-rock interactions along the subduction interface (Gyomlai et al., 2023a). More
101 accurate age constraints were obtained by combining Rb-Sr dating of white mica with initial
102 Sr isotope constraints of epidote and apatite in metamafic rocks from Syros (Barnes et al.,
103 2024).

104
105 These studies highlight the great potential of in-situ mica Rb-Sr geochronology by LA-ICP-
106 MS/MS to investigate different rock-types and geological questions (e.g., Redaa et al., 2022;
107 Wang et al., 2022; Zametzer et al., 2022; Huang et al., 2023; Giuliani et al., 2024). Yet, it
108 remains challenging to date young (i.e., Cenozoic) metamafic and metasomatic lithologies with
109 low Rb contents (e.g., <30 ppm in mafic rocks) and associated low Rb/Sr micas where ingrowth
110 of radiogenic Sr is limited. In this contribution, we address the limitations of in-situ Rb-Sr
111 dating of white mica in young metamafic and metasomatic rocks and propose strategies to
112 obtain robust Rb-Sr ages using laser ablation methods. We present new data of 10 samples
113 from Syros Island (Kampos Belt and Megas Gialos area; Greece) and integrate petrographic
114 and textural analysis of HP-LT rocks with laser ablation Rb-Sr analyses of white mica and
115 multi-collector (MC) ICP-MS Sr isotope analyses of epidote (complemented with bulk rock Sr
116 isotopes for some of the samples). Although the general architecture and structural
117 relationships of blueschist- to eclogite-facies rocks in Syros are still debated (e.g., Keiter et al.,
118 2011; Laurent et al., 2018; Kotowski et al., 2022), the subdivision of geological units, P-T
119 conditions and the timing of metamorphic burial and exhumation are well-constrained, making
120 Syros an ideal case study for our purpose. We demonstrate that in these young (Cenozoic)
121 metasomatic and metamafic rocks, anchoring mica-based Rb-Sr isochrons to initial (or
122 ‘common’) $^{87}\text{Sr}/^{86}\text{Sr}$ from a cogenetic phase such as epidote or a geologically meaningful
123 ‘model’ (e.g., Rosel and Zack, 2021) circumvent issues with low Rb-Sr ratios in these rocks.

124
125
126



127
 128 **Figure 1.** A. Simplified geologic map of the Cyclades highlighting the location of Syros Island. B. Simplified
 129 geologic map of Syros Island (modified from Keiter et al., 2011); the study localities are highlighted in red. C.
 130 Zoom in of the Kampos Belt; the study locality is shown in red. D. Field image of an omphacite pod embedded
 131 in a foliated blueschist matrix within the Grizzas shear zone, the former contains some of the studied glaucophane
 132 + phengite dilational veins (sample SYGR41). E. Representative field image of metasomatic rocks from the
 133 Grizzas shear zone; note the occurrence of smeared metagabbro blocks surrounded by metasomatic rinds and
 134 black walls within a foliated blueschist and a chlorite-tremolite schists matrix. F. Orthomosaic image from the
 135 Megas Gialos outcrop (inset from panel B; modified from Muñoz-Montecinos and Behr, 2023). The lower-
 136 hemisphere stereonet depicts the orientation of the veins following the main foliation as well as those sets oblique
 137 to it (dashed white lines illustrate the orientation of conjugated vein sets), represented here by samples SYMG08.3
 138 and SYMG02, respectively. G and H. Examples of dilational veins containing epidote fibers along with phengite.

139 Geological setting

140 Syros Island

141 The HP-LT rocks from Syros Island belong to the Cyclades Blueschists Unit (CBU) cropping
142 out along the Aegean Sea (**Figure 1A and 1B**). The CBU is interpreted to represent exhumed
143 fragments of the subducted Adriatic plate and HP-LT meta-ophiolites of a northward-dipping
144 subduction event between the Eurasian and African plates (Gautier and Brun, 1994; Jolivet et
145 al., 2010; Soukis and Stockli, 2012). The CBU is subdivided into three subgroups (Glodny and
146 Ring, 2022), from which the Top and Middle CBU nappes are relevant for this study. The Top
147 CBU nappe crops out in Syros as a narrow belt, known in the literature as the Kampos Belt, to
148 which one of the study localities belong to: the Grizzas shear zone (**Figure 1C**). It is composed
149 of abundant metavolcanic materials with a bimodal composition (mafic and felsic) along with
150 metagabbros, serpentinites, tremolite-chlorite, talc- and garnet schists (Keiter et al., 2011). The
151 Kampos Belt lithologies reached peak blueschist- to eclogite-facies conditions of 480–560°C
152 and 1.6–2.2 GPa (e.g., Trotet et al., 2001; Laurent et al., 2018; Cisneros et al., 2020). The
153 Middle CBU nappe is the most abundant unit and is mainly composed of a relatively coherent
154 intercalation of marbles, metasediments and metabasites (**Figure 1B**). This latter lithotype
155 represents the studied lithology at the Megas Gialos locality (**Figure 1B and 1F**), displaying a
156 pervasive exhumation overprint transitioning from blueschist- to greenschist-facies from 450
157 to 400 °C and 1.4 to 1.0 GPa (Cisneros et al., 2020). These retrograde metamorphic conditions
158 are associated with transient brittle fracturing and dilational veining (Muñoz-Montecinos and
159 Behr, 2023), from which the investigated samples from Megas Gialos were collected.

160 The pre-subduction architecture of the CBU resulted from Triassic rifting of the basement
161 accompanied by deposition of passive margin sediments and carbonates (Keay, 1998; Seman
162 et al., 2017). Rifting occurred at c. 80 Ma, thinning the lithosphere and producing small-scale
163 oceanic basins along with passive margin depocenters (Keiter et al., 2011; Cooperdock et al.,
164 2018; Kotowski et al., 2022). In the Kampos Belt (Grizzas locality), U-Th-Pb SHRIMP zircon
165 analyses in a metagabbro and a meta-plagiogranitic dike reveal two age populations, one at c.
166 80 Ma and a second one at 52.4 ± 0.8 Ma (Tomaschek et al., 2003). The older age likely reflects
167 the magmatic crystallization, whereas the younger one dates the HP-LT peak metamorphism.
168 Phengite and multi-mineral Rb-Sr (e.g., white mica + epidote + glaucophane +/- omphacite +/-
169 garnet), phengite Ar-Ar and garnet Lu-Hf ages (mostly from the Lia side, hereafter referred to
170 as the Western Kampos Belt) are in the range of 55 to 44 Ma, and were interpreted to reflect
171 the timing of prograde-to-peak HP-LT metamorphism (see Kotowski et al., 2022 and
172 references therein). Similar peak ages of 51.8 ± 0.1 Ma were obtained by Lu-Hf geochronology
173 of garnet in a metasedimentary rock from the Fabrikas outcrop in south Syros Island (Tual et
174 al., 2022). The initial stage of exhumation under blueschist-facies conditions likely began at c.
175 44 Ma and transitioned to greenschist-facies conditions between 34 and 20 Ma based on Ar-Ar
176 and Rb-Sr multi-mineral (e.g., white mica + epidote + albite) geochronology (e.g. Putlitz et al.,
177 2005; Uunk et al., 2018; Glodny and Ring, 2022 and references therein). Gyomlai et al. (2023a)

178 obtained three in-situ mica Rb-Sr ages from an outcrop within the Kampos belt (Lia side) in
179 the range of 36.3 ± 5.1 Ma to 36.1 ± 4.7 Ma, inferred to date metasomatism of metamafic rocks
180 during blueschist- to greenschist-facies exhumation. The authors also reported older ages in the
181 range of 52.5 ± 11.6 to 39.8 ± 7.4 Ma (Kampos belt, Lia side), but it is unclear whether these
182 ages represent metasomatism and/or mineral (re)crystallization during peak metamorphism or
183 retrogression during HP to late exhumation. Multi-mineral and in-situ white mica Rb-Sr and
184 Ar-Ar dating in the Middle CBU nappe yielded peak HP-LT metamorphism ages of 45 to 37
185 Ma, whereas the pervasive blueschist- to greenschist-facies metamorphism is dated at c. 39 to
186 19 Ma (Glodny and Ring 2022; Barnes et al., 2024; Kotowski et al., 2022 and references
187 therein).

188 Samples and Petrography

189 In this section, we present key petrographic observations of the 10 samples from the Syros
190 Island that have been selected for Rb-Sr dating (**Table 1**), emphasizing the textural context of
191 white mica and epidote. Two additional samples (SYGR50 and SYGR44) have been analyzed
192 for epidote $^{87}\text{Sr}/^{86}\text{Sr}$ only. The investigated samples were carefully selected in order to
193 constrain the timing of fluid-rock interaction (metasomatism and veining) and to evaluate the
194 significance of $^{87}\text{Sr}/^{86}\text{Sr}$ isotopic values for anchoring white mica Rb-Sr isochrons. We targeted
195 our samples based on the presence of white mica in apparent textural equilibrium with epidote
196 (where present) and, for the Grizzas samples, the apparent absence of greenschist-facies
197 overprinting.

198
199 The samples coded SYGR (seven out of nine samples were dated) all belong to the Grizzas
200 locality in the easternmost part of the Kampos Belt (**Figure 1B and 1C**). These samples were
201 collected along a north-dipping shear zone (hereafter referred to as the Grizzas shear zone),
202 which juxtaposes a massive to variably strained metagabbro and blueschist-facies igneous
203 breccia, representing a region of high and localized strain (**Figure 1C**; see also Keiter et al.,
204 2011). Samples SYGR36 and SYGR44 correspond to relict (partially digested) blueschist
205 blocks, while sample SYGR50 represents a pristine, low-strain metagabbro. SYGR37 and
206 SYGR38 represent the metasomatized mafic matrix wrapping around the metagabbro and
207 blueschist blocks (i.e., metasomatic rinds in **Figure 1D**), whereas sample SYGR42 is an altered
208 metagabbro (see **Table 1** for a summary of the studied samples). For comparison, a
209 metasedimentary rock sample (SYGR45) from a ~ 70 cm thick discrete layer within the shear
210 zone as well as a felsic pod (sample SYGR58) contained within a moderately-strained meta-
211 igneous breccia (e.g., Keiter et al., 2011), were also targeted for dating. We emphasize the
212 occurrence of dilational phengite + glaucophane veins (such as sample SYGR41) cross-cutting
213 omphacite pods (**Figure 1E**). The samples coded SYMG were collected from a retrograde
214 greenschist-to-blueschist-facies sliver located in the Megas Gialos locality (**Figure 1F**). The
215 selected vein samples SYMG02 and SYMG08.3 (**Figure 1G and 1H**) formed as dilational
216 fractures related to the ascent of deep subduction zone fluids towards the base of the fore arc
217 during the latest stages of HP-LT exhumation and extension (e.g., Muñoz-Montecinos and

218 Behr, 2023). Sample SYMG07 represents the greenschist host rock associated with the vein
 219 samples SYMG02 and SYMG08.3

Table 1. Sample summary

Sample ID	Rock type and general structure	Mineral assemblage	Analysed microdomain
<i>Grizzas shear zone (NE Syros)</i>			
<i>Blueschist-facies</i>			
SYGR36	Strongly foliated blueschist block	Gln + Ep + Wm + Gte + Omp + Rt	Wm defining the main foliation and pressure shadows around Gte
SYGR37	Moderate to strongly foliated metasomatic rind	Gln + Ep + Wm + Chl	Wm defining the main foliation
SYGR38	Weakly foliated metasomatic rind	Gln + Ep + Wm + Chl	Randomly oriented and interlocked Wm and Ep
SYGR41	Dilational vein	Gln + Wm	Randomly oriented laths of Wm
SYGR42	Moderately foliated metagabbro	Gln + Wnc + Omp + Ep + Wm + Rt	Shear bands defining the main foliation
SYGR44	Moderately foliated blueschist block	Gln + Lws (now Ep + Wm) + Wm + Gte + Rt	Ep replacing Lws pseudomorphs
SYGR45	Foliated metasediment	Wm + Gln + Gte + Ep + Tur	Wm aligned and oblique according to the main foliation
SYGR50	Weakly to moderately foliated metagabbro	Omp + Ep + Gln + Wm	Ep defining the main foliation and within boudin necks
SYGR58	Moderately foliated felsic pod	Qz + Wm	Wm aligned and oblique according to the main foliation
<i>Megas Gialos (SE Syros)</i>			
<i>(HP)Greenschist-facies</i>			
SYMG02	Dilational vein	Qz + Ep + Wm + Ab	Ep fibers and Wm laths in close contact
SYMG07	Moderately to strongly foliated	Ep + Ab + Chl + Act + Wm + Ttn	Ep and Wm defining the main foliation
SYMG08.3	Dilational vein	Qz + Ep + Wm	Ep fibers and Wm laths in close contact

220

221 *Table 1. Summary of the samples selected for this study as well as their corresponding rock type, mineral*
 222 *assemblage (major minerals) and analyzed microdomains. Mineral abbreviations are from Whitney and Evans*
 223 *(2010). Chl – chlorite; Ep – epidote; Gln – glaucophane; Grt – garnet; Omp – omphacite; Qz – quartz; Ttn –*
 224 *titanite; Tur – tourmaline; Wm – white mica; Wnc – winchite.*

225 **Blueschists, blueschist-facies metagabbro and greenschist**

226 Samples SYGR36 and SYGR44 are relict blueschist blocks within a metasomatized sheared
 227 matrix. Glaucophane, together with white mica and epidote define the penetrative foliation.
 228 Texturally, white mica occurs as medium-grained laths and displays no evidence of kinks,
 229 undulose extinction or fish. In sample SYGR36, white mica also occurs within pressure
 230 shadows (**Figure 2A**) and boudin necks around garnet as well as oblique to the main foliation.
 231 No significant zoning patterns in major elements were observed (**Supplementary Figure S1A-**
 232 **F**; see also **Figure S2** for white mica mineral chemistry data). Mostly, white mica grains
 233 defining the main foliation as well as those spatially related to pressure shadows were targeted
 234 for dating. Sample SYGR44 texturally preserves lozenge-shaped lawsonite pseudomorphs now
 235 composed of strain-free epidote (targeted for $^{87}\text{Sr}/^{86}\text{Sr}$ analyses) and white mica
 236 (**Supplementary Figure S1G**).

237

238 Sample SYGR50 is a low-strain metagabbro composed of coarse-grained clinopyroxene
239 pseudomorphs (now glaucophane, winchite and omphacite) in a matrix of epidote. The (weak)
240 foliation is defined by elongated tabular crystals of epidote and subordinate white mica. Boudin
241 necks within large porphyroclasts are filled by epidote, white mica and garnet (**Supplementary**
242 **Figure S1H**). In this sample, epidote crystals defining the foliation and filling the boudin necks
243 were targeted for $^{87}\text{Sr}/^{86}\text{Sr}$ analyses. Overall, this sample represents the weakly-metasomatized
244 analogue of the altered metagabbro sample SYGR42.

245

246 Sample SYMG07 is a coarse-grained greenschist and represents the host rock associated with
247 the vein samples SYMG02 and SYMG08.3. The main foliation is defined by amphibole and
248 epidote, oriented laths of chlorite and white mica as well as stretched albite (**Figure 2B**).
249 Phengite grains in the matrix exhibit weak core-mantle zoning patterns noticeable in back-
250 scattered electron imaging, reflecting mild variations in $\text{Mg}^{2+}/(\text{Fe}^{2+} + \text{Mg}^{2+})$ ratios (XMg)
251 (**Supplementary Figure S1B**; see also **Figure S2**). The core of large white mica grains was
252 targeted for dating, while the foliated matrix epidote was targeted for $^{87}\text{Sr}/^{86}\text{Sr}$ determinations,
253 since these are interpreted as part of an equilibrium assemblage.

254 **Metasomatic rinds, altered metagabbro and veins**

255 Samples SYGR37 and SYGR38 represent the matrix wrapping around metagabbro and
256 blueschist blocks. These samples are coarse-grained, foliated schists composed mainly of
257 glaucophane, epidote, phengite and chlorite. White mica from both metasomatic rinds are
258 medium to coarse-grained and occur in sharp contact with glaucophane and epidote, displaying
259 no significant chemical zoning patterns in major elements nor textural evidence of
260 recrystallization (**Figures 2C and 2D**; see also **Figure S2**). Sharp contacts between white mica
261 and epidote suggest textural equilibrium between them (**Supplementary Figure S1C**). Thus,
262 we targeted these microdomains for white mica dating and $^{87}\text{Sr}/^{86}\text{Sr}$ determinations.

263

264 Sample SYGR42 is an altered metagabbro composed of porphyroclasts of Na-Ca amphibole
265 and omphacite after igneous clinopyroxene in a matrix of epidote, white mica and glaucophane
266 (**Figure 2E**). Two generations of epidote, spatially associated with two distinct microdomains,
267 are observed. The first epidote generation grew as fine-grained, now heavily smeared crystals
268 occupying the interstitial matrix between porphyroclasts. This texture likely reflects epidote
269 growth after igneous plagioclase and subsequent deformation. The second epidote generation
270 grew in microdomains where a discontinuous foliation composed of tabular glaucophane and
271 epidote in sharp contact with white mica, wrapped around porphyroclasts and the fine-grained
272 epidote matrix. Within this second microdomain, white mica is medium- to coarse-grained and
273 displays evidence of recrystallization and subgrains. For this reason, coarse-grained white mica
274 crystals displaying no textural evidence for recrystallization, such as subgrains, kinks and
275 undulose extinction, were carefully selected for dating, whereas euhedral and tabular epidote
276 crystals in sharp contact with white mica crystals were targeted for $^{87}\text{Sr}/^{86}\text{Sr}$ analysis.

277

278 Sample SYGR41 is a glaucophane + white mica dilational vein cross-cutting an omphacitite
279 pod. These veins display up to centimeter-sized and randomly oriented laths of white mica
280 (**Figure 2F**) displaying no evidence of deformation nor significant chemical zoning
281 (**Supplementary Figure S1D**).

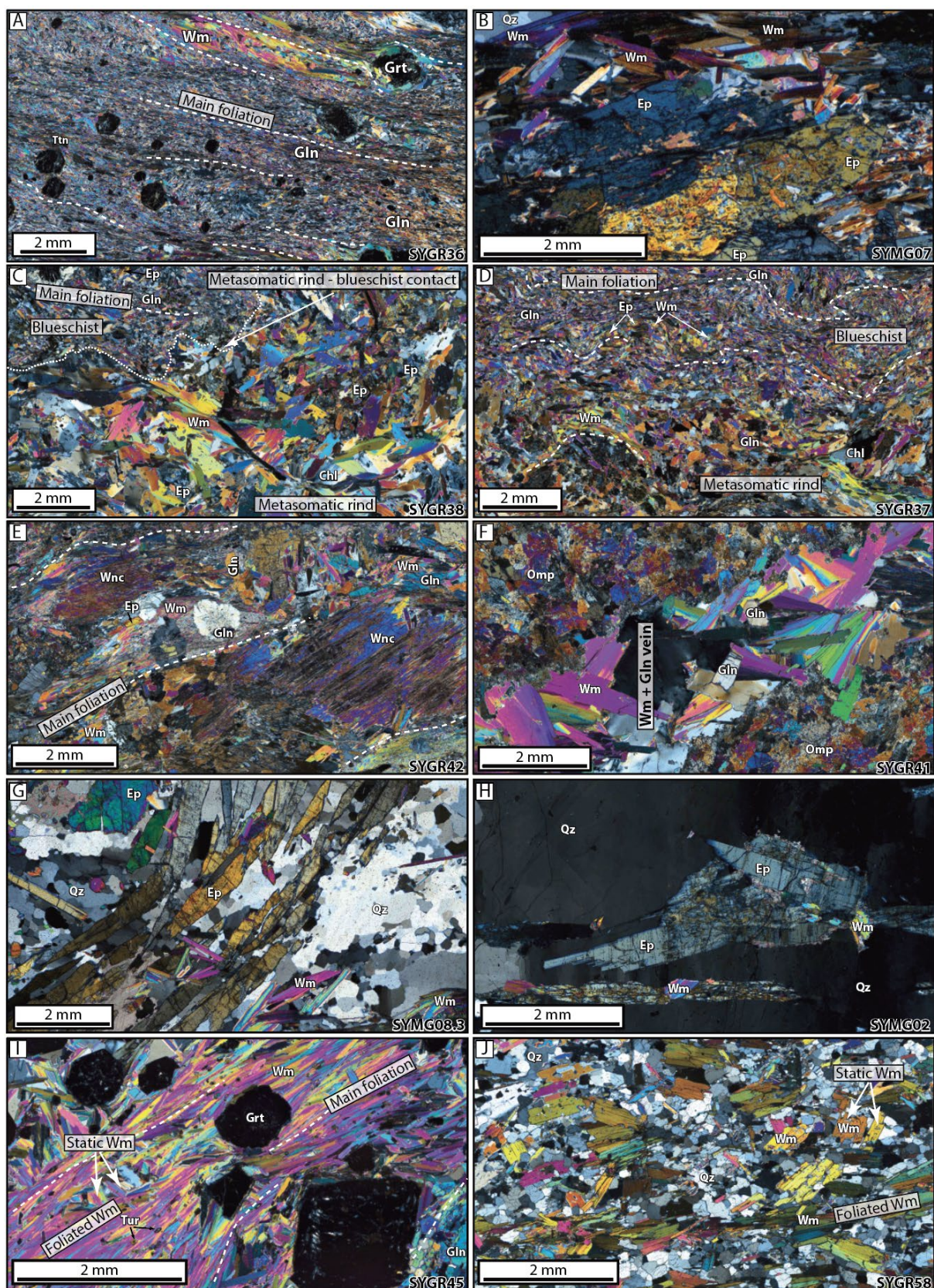
282
283 Samples SYMG02 and SYMG08.3 are dilational veins crosscutting the foliated greenschist
284 hosts. Elongated epidote crystals occur spatially associated with white mica in sharp contact
285 suggesting contemporaneous precipitation from a fluid phase (**Figures 2G and 2H**). White
286 mica occurs as euhedral, hundreds of μm long laths and correspond to strain free crystals with
287 no to faint chemical zoning (**Supplementary Figures S1E and S1F**). Thus, the most coarse
288 and pristine (e.g., unfractured) crystals were selected for white mica dating and epidote
289 $^{87}\text{Sr}/^{86}\text{Sr}$ analyses.

290 **Metasedimentary rock and felsic pod**

291 Sample SYGR45 is a well foliated garnet, glaucophane, tourmaline, mica schist with minor
292 epidote (**Figure 2I**). Texturally, the foliated white mica generation is apparently overgrown by
293 a second, static generation characterized by laths oriented oblique to the main foliation (**Figure**
294 **2E**). To avoid potentially retrograde rims, cores of large crystals defining the pervasive
295 foliation and those of crystals oblique to it were targeted for dating. However, the resulting
296 ages for these two white mica generations were indistinguishable within uncertainty, therefore
297 the final age for this sample was calculated by clustering both datasets (see below).

298
299 Sample SYGR58 is a felsic pod contained within the blueschist-facies meta-igneous breccia.
300 They are composed mostly of quartz and phengite and subordinate epidote and garnet, the latter
301 typically replaced by chlorite. A first white mica generation defines the foliation, whereas a
302 second generation of laths are oriented oblique to it (**Figure 2J**). Although the two white mica
303 generations were separately targeted for dating, the resulting ages overlap and were merged for
304 the final sample age calculation (see below).

305
306
307
308
309
310
311
312
313



314
 315
 316
 317
 318
 319
 320

Figure 2. Photomicrographs (crossed polars) of the dated samples. *A.* General overview of the blueschist block sample SYGR36 emphasizing the distribution of white mica along the foliation and typically around garnets forming pressure shadows. *B.* General fabric of the greenschist sample SYMG07 displaying the association between foliated epidote and white mica. Due to the significant amount of inclusions within epidote, only the inclusion-free regions were targeted for laser ablation MC-ICP-MS analysis. *C.* Contact between altered blueschist and metasomatic rind in sample SYGR38; note the relatively curvy-sharp contact between these two

321 domains as well as the relatively larger abundance of coarse-grained white mica in the latter. D. Contact between
322 altered blueschist and metasomatic rind in sample SYGR37. In this case, the contact is moderately- to highly-
323 strained resulting in a more diffuse appearance. E. Metasomatized metagabbro sample SYGR42 displaying
324 clinopyroxene pseudomorph porphyroclasts (now replaced by amphibole) in a foliated matrix composed of white
325 mica, glaucophane and epidote. F. Dilational vein cross-cutting an omphacitite pod (sample SYGR41) with
326 strain-free, millimeter-sized white mica crystals in association with glaucophane. G. Dilational white mica +
327 epidote + quartz vein (sample SYMG08.3) with a texture characterized by epidote fibers and white mica laths. H.
328 Dilational white mica + epidote + quartz vein (sample SYMG02) displaying coarse-grained epidote in sharp
329 contact with finer-grained white mica. I. Metasedimentary rock sample SYGR45 highlighting white mica crystals
330 oriented parallel and oblique (static) to the main foliation as well as developing pressure shadows around garnet.
331 J. Felsic pod sample SYGR58 highlighting the distribution of white mica along the main foliation as well as some
332 grains oriented oblique to it in a matrix of quartz.

333 **Methods**

334 **Laser ablation MC-ICP-MS**

335 In-situ Sr isotope analyses of epidote were undertaken in two separate sessions (March 2023
336 and February 2024) using an ASI RESolution 193 nm excimer laser ablation system interfaced
337 to a Nu Plasma II MC-ICP-MS at ETH Zürich following a similar approach from Fitzpayne et
338 al. (2023) and Pimenta Silva et al. (2023). Analytical conditions included 80-100 μm spot size,
339 a repetition rate of 5 Hz (Mar-23) and 10 Hz (Feb-24), and laser fluence of ~ 4.0 (Mar-23) and
340 2.5 J cm^{-2} (Feb-24). Each analysis consisted of a sequence of 40 seconds of ablation and 15
341 seconds of washout followed by 30 seconds of gas blank measurement. Total Sr signals varied
342 widely from ~ 1 to 15 V depending on the sample (**Supplementary Table S1**). Data reduction,
343 including corrections for isobaric interferences (Kr, Ca dimers, Ca argides, Rb) and
344 instrumental mass bias was performed using Iolite 4 (Paton et al., 2007, Paton et al., 2011).
345 Instrumental drift was evaluated by repeated measurement of clinopyroxene BB-1 (Neumann
346 et al., 2004; Fitzpayne et al., 2020), which was ablated every block of 15 unknowns including
347 secondary clinopyroxene standards (JJG1414; YY09-04; YY09-47; YY12-01) from Zhao et
348 al. (2020) (results included in **Supplementary Table S1**). All the data are reported relative to
349 BB-1 of $^{87}\text{Sr}/^{86}\text{Sr}$ of 0.704468 (Fitzpayne et al., 2020) via standard bracketing. $^{84}\text{Sr}/^{86}\text{Sr}$ of
350 clinopyroxene standards and epidote unknowns are generally within uncertainty of the natural
351 ratio (~ 0.0565). $^{87}\text{Rb}/^{86}\text{Sr}$ ratios are negligible (typically < 0.001), which makes corrections for
352 ^{87}Sr ingrowth insignificant. Therefore, the reported Sr isotope ratios are considered to be equal
353 to the initial Sr isotope ratios at time of epidote crystallization.

354 **Laser ablation ICP-MS/MS**

355 In-situ Rb-Sr isotopic analyses of white mica in thin section were undertaken during two
356 sessions (October 2022 and May 2023) using an ASI RESolution 193 nm excimer laser probe
357 interfaced to an Agilent 8800 ICP-MS/MS at ETH Zürich following the procedure outlined in
358 Giuliani et al. (2024) and Ceccato et al. (2024), which builds up on the pioneering work of
359 Zack and Hogmalm (2016) and Hogmalm et al. (2017). The mass spectrometer was first tuned
360 in single-quad mode (i.e. no gas in the collision cell) to optimize the Rb and Sr signals by
361 ablating NIST612. Oxide production rate based on measurement of ThO/Th in NIST612 was

362 $\leq 0.2\%$. After introducing ultrapure N_2O gas ($>99.99\%$) in the reaction cell (flow rate of 0.23-
363 0.25 mL min^{-1}), a second tuning step was undertaken by ablating NIST610 to maximize
364 production of SrO^+ ions while maintaining high sensitivity for Rb^+ ions. Interaction of Sr^+ ions
365 with N_2O resulted in conversion of $\sim 89\%$ of Sr^+ ions to SrO^+ based on monitoring of masses
366 88 (Sr^+), 104 (SrO^+) and 105 (SrOH^+). No RbO^+ was detected. Analytical conditions for mica
367 analyses included 80-100 μm spot size, a pulse rate of 5 Hz, and laser fluence of $\sim 3.5\text{-}4.0\text{ J cm}^{-2}$.
368 Each analysis consisted of a sequence of 40 seconds of ablation and 15 seconds of washout
369 followed by 30 seconds of gas blank measurement. Dwell times were of 100 ms for ^{85}Rb ,
370 $^{86}\text{Sr}^{16}\text{O}$ and $^{87}\text{Sr}^{16}\text{O}$, 50 ms for ^{86}Sr and $^{87}(\text{Sr}+\text{Rb})$, 20 ms for ^{88}Sr , $^{88}\text{Sr}^{16}\text{O}$ and $^{88}\text{Sr}^{16}\text{OH}$, and
371 10 ms for other elements (e.g., Ca, Ti, Ni, Ce, Yb, Th), which were monitored to assess
372 potential contamination by extraneous material. Data reduction was performed using the “Rb-
373 Sr isotopes” data reduction scheme in Iolite 4 (Paton et al., 2011). Instrumental drift and
374 quantification of $^{87}\text{Sr}/^{86}\text{Sr}$ and ‘uncorrected’ $^{87}\text{Rb}/^{86}\text{Sr}$ were undertaken by repeated ablation of
375 NIST610, which was measured every block of 15 unknowns including in-house mica standards
376 (see below). Natural glass standards BCR-2G and BHVO-2G were also analyzed as a quality
377 measure of the Sr isotope analyses and returned values broadly consistent with accepted values
378 (**Supplementary Table S2**). NIST610 is a synthetic glass with different ablation properties
379 than mica and, therefore, this approach provides biased (i.e. ‘uncorrected’) $^{87}\text{Rb}/^{86}\text{Sr}$ ratios in
380 mica analyses (e.g., Redaa et al., 2021). Correction of NIST610-based ‘uncorrected’ $^{87}\text{Rb}/^{86}\text{Sr}$
381 in the mica unknowns was performed following the method outlined by Giuliani et al. (2024).
382 The calculated age of an in-house mica standard from the Wimbledon kimberlite (South
383 Africa), which has a robustly constrained Rb-Sr age of $114.5 \pm 0.8\text{ Ma}$ (2σ) based on isotope
384 dilution analyses (Sarkar et al., 2023) and exhibits large variation in Rb/Sr (almost 3 orders of
385 magnitude), was employed to calculate a correction factor that is then employed to obtain the
386 final $^{87}\text{Rb}/^{86}\text{Sr}$ in the mica unknowns. The validity of this approach was confirmed by analyses
387 of micas from the Bultfontein kimberlite (South Africa) and Mount Dromedary monzonite
388 (MD-2; Australia) which returned Rb-Sr ages that are indistinguishable from solution-mode
389 Rb-Sr and Ar-Ar analyses of mica on the same sample: $88.3 \pm 0.2\text{ Ma}$ (Fitzpayne et al., 2020),
390 and $99.20 \pm 0.08\text{ Ma}$ (Phillips et al., 2017), respectively (**Supplementary Table S2**). Time-
391 resolved spectra of mica unknowns and reference materials were screened to remove
392 anomalous regions based on e.g., low concentrations of Rb and high concentrations of Sr, Ca,
393 Ce and/or other incompatible trace elements. Analyses with total signals of less than 10 seconds
394 (after screening) and with anomalously low contents of Rb or high contents of Sr (and Ca),
395 often resulting in $^{87}\text{Rb}/^{86}\text{Sr} < 2.5$, as well as analyses with large $^{87}\text{Sr}/^{86}\text{Sr}$ uncertainties and data
396 points that plotted distinctly off the isochron were not included in the Nicolaysen diagrams
397 (**Supplementary Table S3**). All the isochron ages were calculated using IsoplotR (Vermeesch,
398 2018) and the ^{87}Rb decay constant of $1.3972 \times 10^{-11}\text{ a}^{-1}$ (Villa et al., 2015). Trace element
399 concentrations were not quantified.
400

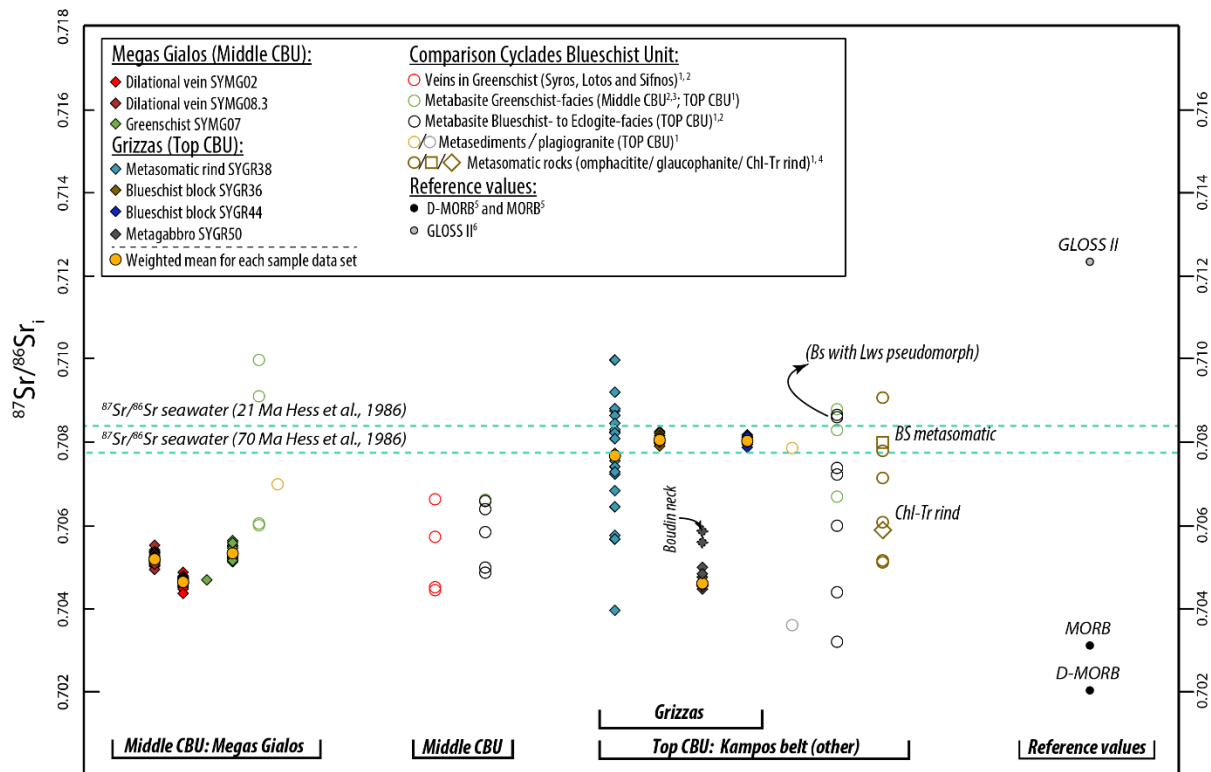
401 Results

402 Epidote Sr isotopes

403 The $^{87}\text{Sr}/^{86}\text{Sr}$ ratios were measured by laser ablation MC-ICP-MS in 5 of the 10 samples
404 employed for mica Rb-Sr geochronology. Two additional samples (SYGR44; SYGR50) were
405 also included to corroborate the signature of the blueschist and metagabbro rocks. For
406 comparison, we also present isotope-dilution Sr isotope data in samples from the Megas Gialos
407 locality, including the 3 samples analyzed for epidote and mica Rb-Sr isotopes. A summary of
408 the new and available Sr isotope data for epidote is reported in **Figure 3** and the full datasets,
409 including bulk rock Sr and Nd isotopic compositions, are included in **Supplementary Tables**
410 **S1 and S4**.

411
412 At Grizzas (Kampos belt), the two blueschist samples (SYGR36 and 44) show very small
413 ranges in epidote $^{87}\text{Sr}/^{86}\text{Sr}$ compositions (see **Supplementary Figure S3**) with
414 indistinguishable weighted means of 0.70805 ± 0.00006 (2SE; $n = 12$) and 0.70802 ± 0.00005
415 (2SE; $n = 18$; **Table 2 and Supplementary Figure S3**). The other two Grizzas samples (the
416 metasomatic rind SYGR38 and the metagabbro SYGR50) exhibit larger isotopic variability.
417 The $^{87}\text{Sr}/^{86}\text{Sr}$ in sample SYGR38 vary widely between 0.70426 ± 0.00008 and $0.710002 \pm$
418 0.00008 ($n = 22$) with no statistically distinct populations (**Figure 3**). The weighted mean
419 (although statistically meaningless) is similar to those of SYGR36 and SYGR44: $0.70767 \pm$
420 0.00058 . In sample SYGR50, 16 epidote grains parallel to the foliation yield a restricted range
421 in Sr isotope values corresponding to a weighted mean of 0.70460 ± 0.00004 , which is
422 substantially less radiogenic than the blueschist samples from Grizzas, although similar to the
423 lowest $^{87}\text{Sr}/^{86}\text{Sr}$ of sample SYGR38. Four epidote grains within boudin necks of sample
424 SYGR50 show more radiogenic values of up to 0.70585 ± 0.00020 .

425
426 Epidote in the three samples from Megas Gialos show very limited within-sample $^{87}\text{Sr}/^{86}\text{Sr}$
427 variability with weighted means of 0.70466 ± 0.00004 ($n = 24$) for SYMG02; $0.70534 \pm$
428 0.00005 ($n = 25$) for SYMG07 and 0.70520 ± 0.00005 ($n = 31$) for SYMG08.03 The epidote
429 Sr isotope compositions are not correlated with the lithology as the greenschist sample
430 SYMG07 has the same $^{87}\text{Sr}/^{86}\text{Sr}$ as one of the two dilational veins (SYMG02 and 08.03).
431 Measured (i.e. present-day) $^{87}\text{Sr}/^{86}\text{Sr}$ of bulk rock SYMG07 is 0.705414 ± 0.000008 (2σ s.d. of
432 NBS987 standards measured in the same session), marginally more radiogenic than the
433 SYMG07 epidote, and minimally affected by radiogenic ingrowth (e.g., ~ 0.0002 in 50 Myr)
434 due to low bulk-rock $^{87}\text{Rb}/^{86}\text{Sr}$ of 0.290 (**Supplementary Table S1**). The bulk-rock $^{87}\text{Sr}/^{86}\text{Sr}$
435 of SYMG08.03 (0.705281 ± 0.000006) is almost indistinguishable from the epidote value
436 reported above. The very low $^{87}\text{Rb}/^{86}\text{Sr}$ (0.073) suggests minimal radiogenic Sr ingrowth in
437 this bulk sample.



438
 439 **Figure 3.** Overview of $^{87}\text{Sr}/^{86}\text{Sr}$ in-situ laser ablation MC-ICP-MS epidote data points and comparison to ID-
 440 TIMS (whole rock and multi-mineral) analyses from different localities in Syros. The resulting $^{87}\text{Sr}/^{86}\text{Sr}$ values
 441 are assumed to represent initial ratios due to the lack of Rb in epidote. For comparison, pristine MORB and D-
 442 MORB, as well as compiled trench filling sediments (GLOSS II) along with Cretaceous to Miocene $^{87}\text{Sr}/^{86}\text{Sr}$
 443 seawater values are shown. Uncertainties are smaller than the symbol size. 1 – Glodny and Ring (2022); 2 –
 444 Kotowski et al. (2022); 3 – Bröcker et al. (2013); 4 – Bröcker and Enders (2001); 5 – Salters and Stracke (2004);
 445 6 – Plank (2014).

446 Mica Rb-Sr dating

447 In this section we report the mica Rb-Sr isotope data and describe the related isochronous array
 448 for each sample, complemented in 5 cases by epidote Sr isotope results. The complete white
 449 mica dataset, including Rb and Sr isotope ratios, is provided in **Supplementary Table S3** (see
 450 **Table 2** for a summary of the age data). For each sample we also provide a model age where
 451 the mica Rb-Sr isochron is anchored to an assumed $^{87}\text{Sr}/^{86}\text{Sr}$ value, that is 0.7080 ± 0.0005 for
 452 all the samples from Grizzas, and 0.7050 ± 0.0005 for those from Megas Gialos. For Grizzas,
 453 employing this value is justified by the fact that the weighted mean of epidote Sr isotopes are
 454 ~ 0.708 for three of the four analyzed samples (**Figure 3**; see also the compiled data in **Figure**
 455 **3** for metabasites from the Top CBU), and “unanchored” mica Rb-Sr isochrons are generally
 456 within uncertainty of this value (see below). The epidote and bulk-rock compositions at Megas
 457 Gialos cluster at $^{87}\text{Sr}/^{86}\text{Sr}$ of ~ 0.705 (**Figure 3**) hence providing a robustly constrained initial
 458 Sr composition for anchoring the mica-based Nicolaysen arrays. In the discussion section, we
 459 will address the impact of changing initial (or “common”) $^{87}\text{Sr}/^{86}\text{Sr}$ composition in the
 460 calculated Rb-Sr isochron.

461 **SYGR36**

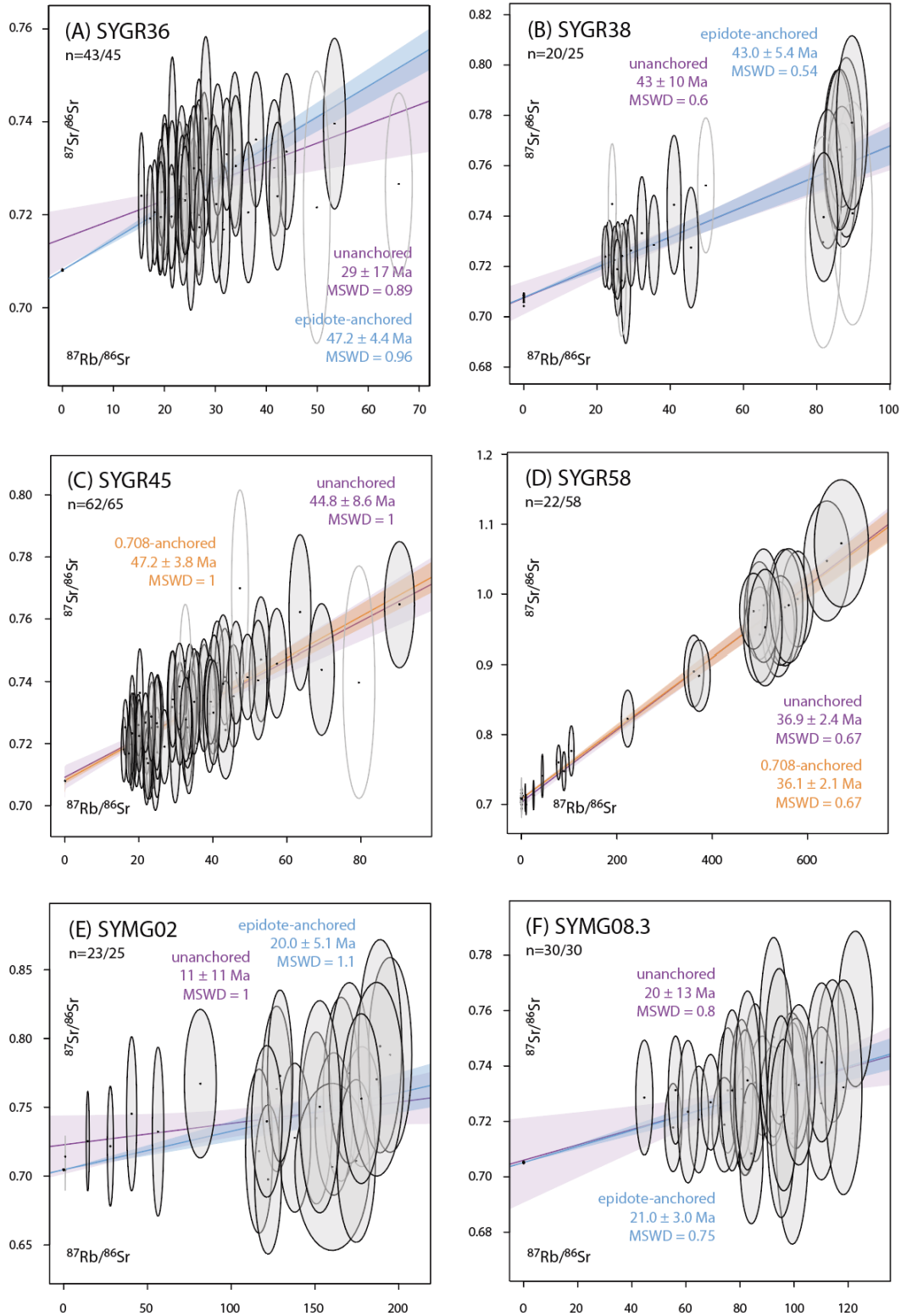
462 White mica in the blueschist block sample SYGR36 show a spread in $^{87}\text{Rb}/^{86}\text{Sr}$ between 15
463 and 53 ($n = 43/45$) associated with variations in $^{87}\text{Sr}/^{86}\text{Sr}$ between 0.7166 and 0.7407 (**Figure**
464 **4A**). The limited Rb/Sr spread results in a poorly defined “unanchored” isochron age of $29 \pm$
465 17 Ma (2SE, MSWD = 0.89, initial $^{87}\text{Sr}/^{86}\text{Sr} = 0.7149 \pm 0.0062$). Anchoring the phengite Rb-
466 Sr data to epidote from the same sample (weighted mean $^{87}\text{Sr}/^{86}\text{Sr} = 0.70805 \pm 0.00006$)
467 provides a rather different (although within uncertainty) and considerably more precise age of
468 47.2 ± 4.4 Ma (2SE, MSWD = 0.96). Assuming a modeled initial $^{87}\text{Sr}/^{86}\text{Sr}$ of 0.7080 ± 0.0005
469 (1s) provides an age of 46.9 ± 5.1 Ma (2s, MSWD = 0.96), overlapping closely with the epidote-
470 anchored isochron age.

471 **SYGR37**

472 White mica grains in the metasomatic rind sample SYGR37 show a slightly larger spread in
473 $^{87}\text{Rb}/^{86}\text{Sr}$ (22-112, $n = 36/38$) and $^{87}\text{Sr}/^{86}\text{Sr}$ (0.7211-0.7676) compared to SYGR36, resulting
474 in a more precise unanchored isochron age of 32.3 ± 7.5 Ma (MSWD = 0.51, initial $^{87}\text{Sr}/^{86}\text{Sr} =$
475 0.7158 ± 0.0059 ; **Supplementary Figure S4**). Anchoring these mica Rb-Sr to modeled initial
476 $^{87}\text{Sr}/^{86}\text{Sr}$ of 0.7080 ± 0.0005 (2SE) yields an older age of 41.1 ± 3.1 Ma (MSWD = 0.66).

477 **SYGR38**

478 White mica in the metasomatic rind SYGR38 shows spreads between 22-90 and 0.7140-0.7771
479 for $^{87}\text{Rb}/^{86}\text{Sr}$ and $^{87}\text{Sr}/^{86}\text{Sr}$, respectively ($n = 20/25$, with 5 analyses excluded based on short
480 signals of less than 10 seconds). The corresponding unanchored isochron age is 43 ± 10 Ma
481 (MSWD = 0.6, initial $^{87}\text{Sr}/^{86}\text{Sr} = 0.7075 \pm 0.0064$; **Figure 4B**). Adding epidote Sr isotopes
482 (weighted mean $^{87}\text{Sr}/^{86}\text{Sr} = 0.70767 \pm 0.00058$ (2SE)) to the mica Rb-Sr isochron yields the
483 same, yet more precise age of 43.0 ± 5.4 Ma (MSWD = 0.54). Using a modeled initial $^{87}\text{Sr}/^{86}\text{Sr}$
484 of 0.7080 ± 0.0005 (2SE) results in a similar age of 42.5 ± 5.5 Ma (MSWD = 0.54). Considering
485 the large spread in epidote $^{87}\text{Sr}/^{86}\text{Sr}$ values (~ 0.7043 to ~ 0.7100), we have also calculated
486 model ages using initial $^{87}\text{Sr}/^{86}\text{Sr}$ of 0.7050 and 0.7100 and these are within uncertainty of each
487 other: 46.5 ± 5.6 Ma (MSWD = 0.57) and 39.8 ± 5.5 Ma (MSWD = 0.57), respectively
488 (**Supplementary Figure S5**).



489
 490 **Figure 4.** Representative laser-ablation ICP-MS/MS Rb-Sr isochrons of white micas from Grizzas (North East
 491 Syros Island, SYGR, A-D) and Megas Gialos (South Syros Island, SYMG, E-F). The size of the ellipses represents
 492 internal 2 SE (standard error), where data points that were excluded from the regression are displayed as empty
 493 ellipses. Isochronous regressions are plotted together with their 95% confidence level envelopes in different
 494 colours based on the employed anchoring technique: purple for mica-only unanchored regressions; blue for
 495 regressions anchored to epidote; orange for regressions anchored to a modelled initial $^{87}\text{Sr}/^{86}\text{Sr}$ of $0.7080 \pm$
 496 0.0005 . The number below the sample labels indicates the number of mica analyses. All plots were generated
 497 using IsoplotR (Vermeesch, 2018).
 498

499 **SYGR41**

500 White mica from the dilational vein SYGR41 show a limited spread in $^{87}\text{Rb}/^{86}\text{Sr}$ between 14-
501 63 ($n = 36/36$) associated with variations in $^{87}\text{Sr}/^{86}\text{Sr}$ between 0.7116 and 0.7498. An
502 unanchored isochron through these data yields an age of 45 ± 11 Ma (MSWD = 0.78, initial
503 $^{87}\text{Sr}/^{86}\text{Sr} = 0.7076 \pm 0.0049$). Anchoring these mica Rb-Sr data to a modeled initial $^{87}\text{Sr}/^{86}\text{Sr}$ of
504 0.7080 ± 0.0005 (1s) yields the same, yet more precise age of 44.7 ± 4.5 Ma (2s, MSWD =
505 0.74).
506

507 **SYGR42**

508 $^{87}\text{Rb}/^{86}\text{Sr}$ and $^{87}\text{Sr}/^{86}\text{Sr}$ ratios in phengites from the metasomatized metagabbro sample
509 SYGR42 range from 27 to 185 and 0.7155 to 0.8162, respectively ($n = 30/30$), and the
510 corresponding unanchored isochrons provides an age of 46 ± 9 Ma (MSWD = 1.3, initial
511 $^{87}\text{Sr}/^{86}\text{Sr} = 0.7090 \pm 0.0079$). Anchoring these mica Rb-Sr data to $^{87}\text{Sr}/^{86}\text{Sr} = 0.7080 \pm 0.0005$
512 (1s) results in an overlapping, although more precise age of 46.6 ± 4.6 Ma (MSWD = 1.2).
513

514 **SYGR45**

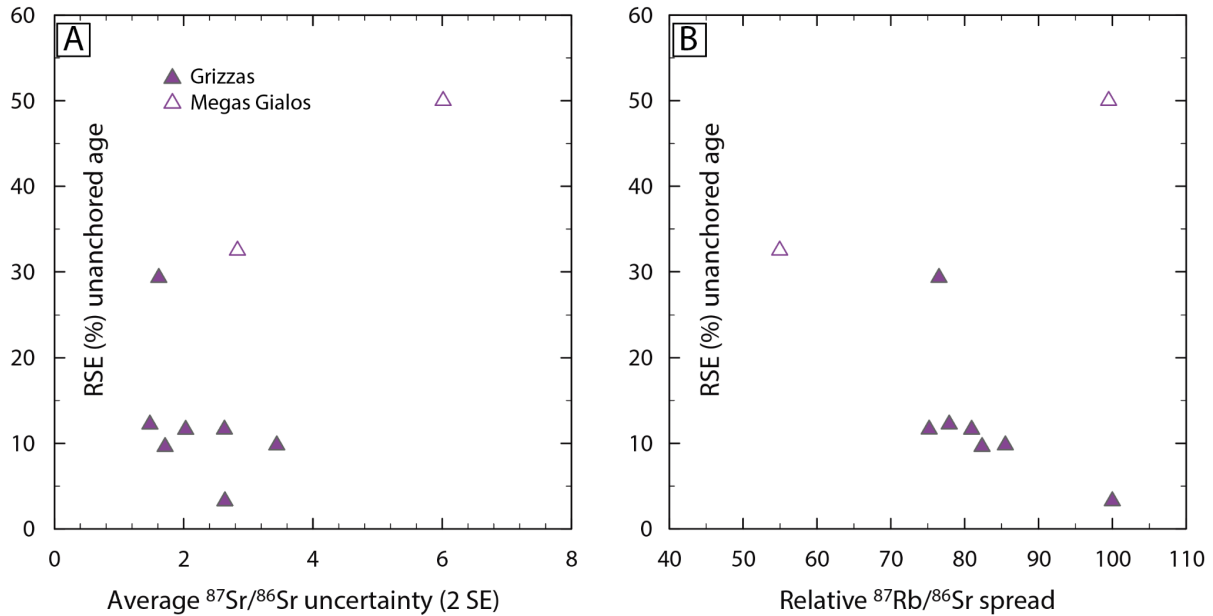
515 Two generations of phengite laths, parallel and oblique to the main foliation, from the
516 metasedimentary rock sample SYGR45 display $^{87}\text{Rb}/^{86}\text{Sr}$ values between 16 and 90 ($n = 62/65$)
517 and a corresponding variation in $^{87}\text{Sr}/^{86}\text{Sr}$ between 0.7134 and 0.7647, with no systematic
518 difference between the two textural types of mica (**Figure 4C**; **Supplementary Table S3**). The
519 resulting unanchored isochron has a slope equivalent to an age of 44.8 ± 8.6 Ma (MSWD = 1,
520 initial $^{87}\text{Sr}/^{86}\text{Sr} = 0.7092 \pm 0.0038$). Anchoring these mica Rb/Sr data to a modeled initial
521 $^{87}\text{Sr}/^{86}\text{Sr}$ of 0.7080 ± 0.0005 (1s) yields a slightly older and more precise age of 47.2 ± 3.8 Ma
522 (MSWD = 1), overlapping with the unanchored age within uncertainty. Using a more
523 radiogenic initial $^{87}\text{Sr}/^{86}\text{Sr}$ of 0.7100 has a small effect on the calculated age (43.2 ± 3.8 ;
524 MSWD = 1).
525

526 **SYGR58**

527 The two textural types of white mica identified in the felsic pod sample SYGR58, parallel and
528 oblique to the main foliation, exhibit indistinguishable Rb-Sr isotope systematics
529 (**Supplementary Table S3**) and are, hence, described together. These white micas show the
530 largest Rb/Sr spread observed in the sample set of between 8 and 671 ($n = 22/58$, where only
531 analyzes with $^{87}\text{Rb}/^{86}\text{Sr} > 2.5$ were considered for the isochron), which is consistent with the
532 felsic nature of this sample. The spread in $^{87}\text{Sr}/^{86}\text{Sr}$ is between 0.670 and 1.073, resulting in
533 precise, although unanchored Rb-Sr age of 36.9 ± 2.4 Ma (MSWD = 0.67, initial $^{87}\text{Sr}/^{86}\text{Sr} =$
534 0.7038 ± 0.0072 ; **Figure 4D**). Anchoring these mica Rb/Sr data to a modeled initial $^{87}\text{Sr}/^{86}\text{Sr}$
535 of 0.7080 ± 0.0005 (2SE) yields a similar age of 36.1 ± 2.1 Ma (2s, MSWD = 0.67).
536

537 **SYMG02**

538 Phengites from the dilational vein sample SYMG02 show a relatively large $^{87}\text{Rb}/^{86}\text{Sr}$ spread
 539 between 14 and 195 ($n = 23/25$) associated with a restricted $^{87}\text{Sr}/^{86}\text{Sr}$ spread between 0.6976
 540 and 0.7944. These data define a meaningless unanchored isochron (age = 11 ± 11 Ma, MSWD
 541 = 1, initial $^{87}\text{Sr}/^{86}\text{Sr} = 0.723 \pm 0.021$; **Figure 4E**). Adding epidote Sr data from the same sample
 542 (weighted mean $^{87}\text{Sr}/^{86}\text{Sr} = 0.70466 \pm 0.00004$) to the mica Rb-Sr isotopes results in a more
 543 meaningful age of 20.0 ± 5.1 Ma (MSWD = 1.1). Using a modeled initial $^{87}\text{Sr}/^{86}\text{Sr}$ anchor of
 544 0.7050 ± 0.0005 (1s) yields a similar age of 19.8 ± 5.2 Ma (2s, MSWD = 1).



545

546 **Figure 5.** Comparison of relative standard error (RSE) of unanchored mica Rb-Sr ages and (A) average $^{87}\text{Sr}/^{86}\text{Sr}$
 547 uncertainties and (B) relative (%) $^{87}\text{Rb}/^{86}\text{Sr}$ spread. The latter was defined as the ratio between the absolute
 548 $^{87}\text{Rb}/^{86}\text{Sr}$ spread and the highest $^{87}\text{Rb}/^{86}\text{Sr}$ value observed for any given sample, resulting in a number between 0
 549 and 100%.

550 **SYMG07**

551 $^{87}\text{Rb}/^{86}\text{Sr}$ and $^{87}\text{Sr}/^{86}\text{Sr}$ values in white mica from the greenschist sample SYMG07 vary
 552 between 75-231 and 0.7199-0.8121, respectively ($n = 12/13$), yielding a meaningless isochron
 553 age of 6.1 ± 31.2 Ma (MSWD = 1.2, initial $^{87}\text{Sr}/^{86}\text{Sr} = 0.749 \pm 0.063$; **Supplementary Figure**
 554 **S4**). Coupling white mica with the SYMG07 epidote data (weighted mean $^{87}\text{Sr}/^{86}\text{Sr} = 0.70534$
 555 ± 0.00005) results in an age of 27.2 ± 8.4 Ma (MSWD = 1.1). An identical age is obtained
 556 using a model initial $^{87}\text{Sr}/^{86}\text{Sr}$ of 0.7050 ± 0.0005 (1s): 27.4 ± 8.4 Ma (2s, MSWD = 1.2).

557

558 **SYMG08**

559 Phengites from dilational vein SYMG08.3 show a spread in $^{87}\text{Rb}/^{86}\text{Sr}$ between 45 and 123 ($n = 30/30$)
 560 associated with variations in $^{87}\text{Sr}/^{86}\text{Sr}$ between 0.7084 and 0.7606 (**Figure 4F**). These
 561 data define an unanchored isochron age of 20 ± 13 Ma (MSWD = 0.8, initial $^{87}\text{Sr}/^{86}\text{Sr} = 0.706$
 562 ± 0.015). Adding Sr epidote data (weighted mean $^{87}\text{Sr}/^{86}\text{Sr} = 0.70520 \pm 0.00005$) to the
 563 phengite Rb/Sr data results in the same, yet more precise age of 21.0 ± 3.0 Ma (MSWD = 0.75).

564 The results hardly change by anchoring the mica Rb/Sr data to a modeled initial $^{87}\text{Sr}/^{86}\text{Sr}$ of
 565 0.7050 ± 0.0005 (2SE): 20.8 ± 3.1 Ma (MSWD = 0.75) (**Supplementary Figure S5**).
 566

Table 2. Summary of epidote Sr isotopes and mica Rb-Sr ages

Sample ID	Epidote $^{87}\text{Sr}/^{86}\text{Sr}$ *			Mica analyses		Mica age, unanchored **				Mica + epidote age (Ma)			Mica age (Ma), anchored ***		
	n	mean	2 SE	n	age (Ma)	2 SE	MSWD	isochron γ intercept	age (Ma)	2 SE	MSWD	age (Ma)	2 SE	MSWD	
<i>Grizzas (NE Syros)</i>															
SYGR36	12	0.70805	0.00006	43/45	29	17	0.89	0.7149 ± 0.0062	47.2	4.4	0.96	46.9	5.1	0.96	
SYGR37	–	–	–	36/38	32.3	7.5	0.51	0.7158 ± 0.0059	–	–	–	41.1	3.1	0.66	
SYGR38	21	0.70767	0.00058	20/25	43	10	0.60	0.7075 ± 0.0064	43.0	5.4	0.54	42.5	5.5	0.54	
SYGR41	–	–	–	36/36	45	11	0.78	0.7076 ± 0.0049	–	–	–	44.7	4.5	0.74	
SYGR42	–	–	–	30/30	46	9	1.30	0.7090 ± 0.0079	–	–	–	46.6	4.6	1.2	
SYGR44	18	0.70802	0.00005	–	–	–	–	–	–	–	–	–	–	–	
SYGR45	–	–	–	62/65	44.8	8.6	1.00	0.7092 ± 0.0038	–	–	–	47.2	3.8	1	
SYGR50	16	0.70460	0.00004	–	–	–	–	–	–	–	–	–	–	–	
SYGR58	–	–	–	22/58	36.9	2.4	0.67	0.7038 ± 0.0072	–	–	–	36.1	2.1	0.67	
<i>Megas Gialos (SE Syros)</i>															
SYMG02	24	0.70466	0.00004	23/25	11	11	1.00	0.723 ± 0.021	20.0	5.1	1.1	19.8	5.2	1	
SYMG07	25	0.70534	0.00005	12/13	6.4	31.2	1.20	0.749 ± 0.063	27.2	8.4	1.1	27.4	8.4	1.2	
SYMG08.3	31	0.70520	0.00005	30/30	20	13	0.80	0.706 ± 0.015	21.0	3.0	0.75	20.8	3.1	0.75	

* laser ablation, multi-collector ICP-MS; complete dataset in Supplementary Table S1
 ** laser ablation, ICP-MS/MS; complete dataset in Supplementary Table S3
 *** anchoring values: 0.7080 ± 0.0005 for SYGR samples; 0.7050 ± 0.0005 for SYMG samples

567
 568

569 Discussion

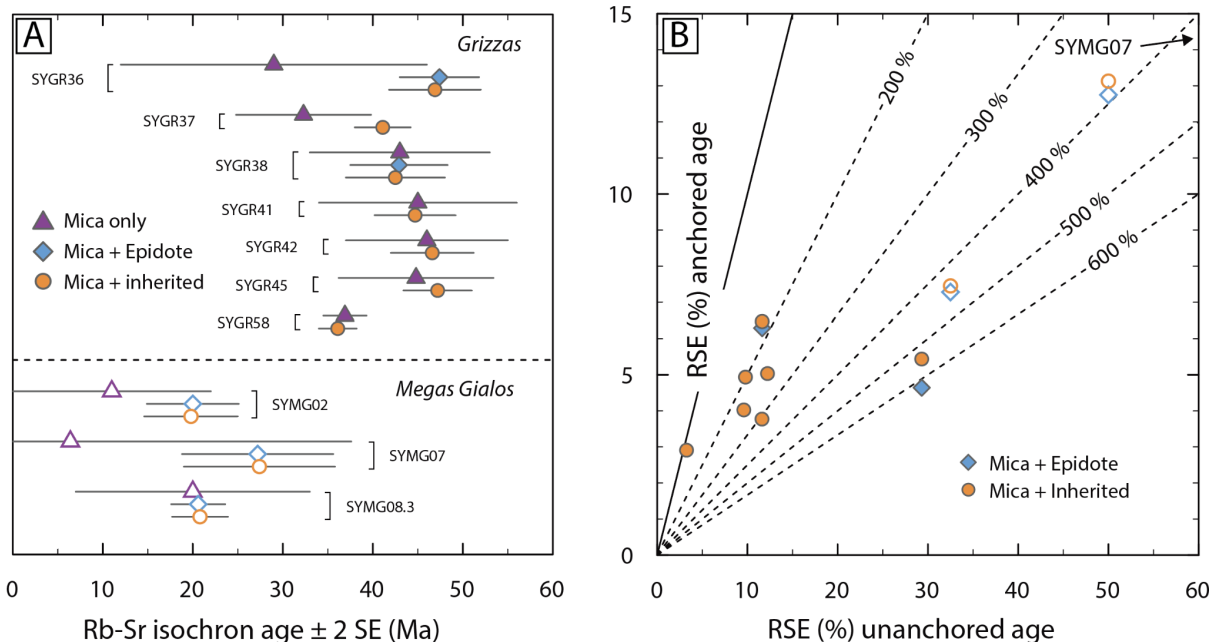
570 Optimal strategies to obtain robust Rb-Sr ages of white 571 mica in young metamorphic rocks by LA-ICP-MS/MS

572 White mica in all the investigated samples, and regardless of their bulk-rock chemistry (i.e.
 573 mafic and metasomatic), exhibit limited spread in Rb/Sr compared to previous studies (e.g.,
 574 Kirkland et al., 2023, Glodny and Ring 2022). Except for the relatively large spread observed
 575 in the felsic sample SYGR58 ($^{87}\text{Rb}/^{86}\text{Sr} = 8$ to 671), the Rb/Sr range of all the other samples
 576 never exceeds one order of magnitude and in some cases less (e.g., $^{87}\text{Rb}/^{86}\text{Sr} = 15$ -53 in
 577 blueschist SYGR36) compared to, for example, the two to three orders of magnitude in
 578 phlogopite from lamproites and kimberlites (Giuliani et al., 2024), or biotite in some
 579 metamorphosed granites (Ceccato et al., 2024). In addition, the combination of relatively low
 580 Rb contents (not quantified but inferred from low Rb/Sr ratios) and geologically young
 581 (Cenozoic) age of the Syros micas did not allow the ingrowth of substantial radiogenic ^{87}Sr as
 582 shown by the low measured $^{87}\text{Sr}/^{86}\text{Sr}$ (generally <0.8 ; **Supplementary Table S3**). Low ^{87}Sr
 583 contents are associated with large uncertainties for $^{87}\text{Sr}/^{86}\text{Sr}$, which systematically exceed 1%
 584 (2SE) for individual measurements (**Supplementary Table S3**). The compounded effects of
 585 low absolute $^{87}\text{Rb}/^{86}\text{Sr}$ values (generally <200 and, for some samples, <100), limited spread in
 586 Rb/Sr and poor precision in the quantification of $^{87}\text{Sr}/^{86}\text{Sr}$ result in large uncertainties
 587 associated with the slopes of unanchored mica Rb-Sr isochrons (**Figure 5A and 5B**). These
 588 uncertainties translate to a poor precision for the related ages with 10-29 %RSE (relative
 589 standard error) in the SYGR samples (except for the felsic sample SYGR58, with an RSE of
 590 3%, i.e. 36.9 ± 2.4 Ma, 2SE), and even larger for the younger SYMG samples (**Figure 6A**).
 591 The inverse correlation between relative $^{87}\text{Rb}/^{86}\text{Sr}$ spread and age uncertainty of unanchored
 592 isochrons in **Figure 5B** exemplifies the impact of Rb/Sr variations on isochron precision. In at

593 least three cases (SYGR36, SYMG02 and SYMG07) these unanchored mica-only isochronous
 594 arrays are not just imprecise, but also rather inaccurate as shown by the substantially older ages
 595 of the mica + epidote isochron for SYGR36 (29 ± 17 Ma vs 47.2 ± 4.4 Ma for SYGR36) or
 596 simply geologically meaningless (11 ± 11 Ma and 6.4 ± 31 Ma for SYMG02 and SYMG07,
 597 respectively; **Table 2**).

598

599 To overcome the limitations in mica Rb-Sr geochronology by LA-ICP-MS/MS due to low
 600 Rb/Sr and/or young ages, the two viable solutions explored here include anchoring the
 601 isochronous arrays to either the Sr isotope composition of a low Rb/Sr phase in textural
 602 equilibrium with mica, such as epidote, or an assumed $^{87}\text{Sr}/^{86}\text{Sr}$ value. The latter approach
 603 effectively provides a “model age” and, while previously explored by Rösler and Zack (2021),
 604 it is rigorously evaluated herein by a systematic comparison with initial Sr isotope constraints
 605 from epidote and bulk rocks. Anchoring mica isochrons to a low Rb/Sr phase has been rarely
 606 applied in mica Rb-Sr geochronology by LA-ICP-MS/MS (Ribeiro et al., 2022; Barnes et al.,
 607 2024; Giuliani et al., 2024), while being widely employed for conventional Rb-Sr dating by
 608 isotope dilution (e.g., Maas, 2003; Glodny et al., 2008; Hyppolito et al., 2016; Angiboust et al.,
 609 2018; Dalton et al., 2020). Comparisons of unanchored mica Rb-Sr ages with those anchored
 610 using mean $^{87}\text{Sr}/^{86}\text{Sr}$ of epidote analyses show an improvement in precision of up to 6 times
 611 (**Figure 6B**) – as well as better accuracy in some cases as shown above for SYGR36. Clearly,
 612 in young HP metamafic rocks such as those from Syros, this approach is recommended to
 613 obtain robust age constraints even when the limited spread in mica Rb/Sr prevents generation
 614 of meaningful isochronous arrays (i.e. SYMG02 and 07).



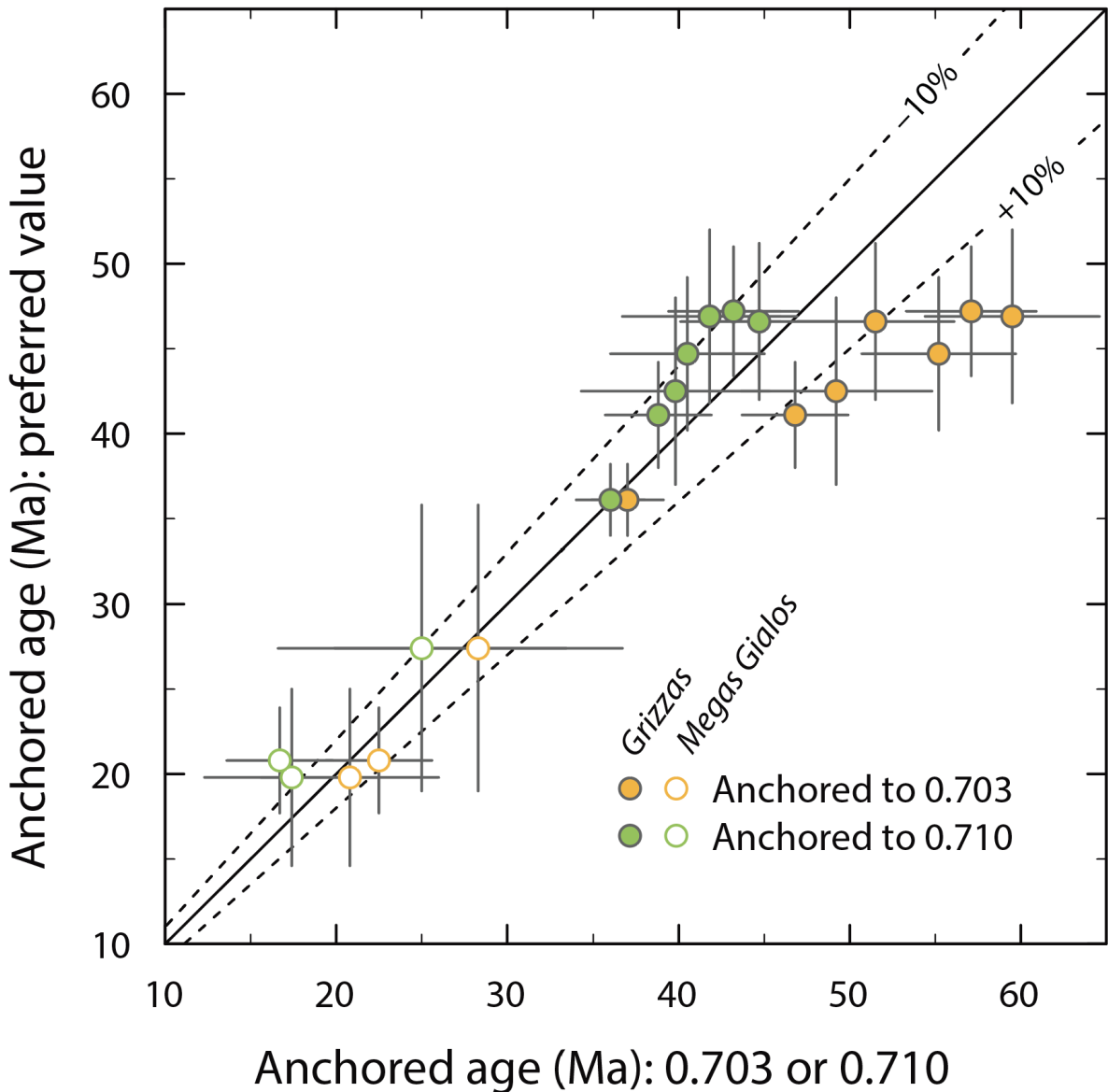
615

616 **Figure 6.** (A) Overview of mica Rb-Sr ages using mica datapoints only (unanchored isochrons, purple), anchoring
 617 to epidote (blue) and anchoring to an assumed initial $^{87}\text{Sr}/^{86}\text{Sr}$ composition (orange). Initial $^{87}\text{Sr}/^{86}\text{Sr}$ was assumed
 618 to be 0.7080 ± 0.0005 (2SE) for Grizzas and 0.7050 ± 0.0005 (2SE) for Megas Gialos (see text). (B) Comparison
 619 of the uncertainties expressed as % RSE (relative standard error) for unanchored mica-only ages and ages
 620 anchored to either epidote or an assumed initial $^{87}\text{Sr}/^{86}\text{Sr}$. Samples from Grizzas and Megas Gialos are shown as
 621 empty and full symbols, respectively. Location of Megas Gialos sample SYMG07 (unanchored age 6.4 ± 31 Ma,
 622 243% RSE) is shown with an arrow.

623 Model ages are also, not surprisingly, substantially more precise than unanchored mica-only
624 Rb-Sr ages. However, their accuracy deserves scrutiny. Where epidote data are available, the
625 model ages calculated in this work can be employed to show the effect of inaccurate initial
626 $^{87}\text{Sr}/^{86}\text{Sr}$ in the isochron ages (**Figure 7**). At Grizzas, epidote $^{87}\text{Sr}/^{86}\text{Sr}$ varies between 0.7043
627 and 0.7100 (all this variation is contained in the metasomatic rind sample SYGR38). Using
628 available bulk rock data for the Kampos Belt (**Figure 3**), this range can be extended downward
629 to ~ 0.7030 , hence effectively bracketing the possible compositions of initial Sr to calculate
630 mica model ages. For simplicity, the same range is employed for Megas Gialos. Beyond the
631 model ages presented in the results section and **Table 2**, for each sample two additional model
632 ages are calculated using an initial $^{87}\text{Sr}/^{86}\text{Sr}$ of 0.7030 ± 0.005 and 0.7100 ± 0.005 , respectively
633 (**Figure 7 and Supplementary Table S5**). In the Grizzas samples, using an initial $^{87}\text{Sr}/^{86}\text{Sr}$ of
634 0.7100 generates model ages that are generally within uncertainty of those where the initial
635 $^{87}\text{Sr}/^{86}\text{Sr}$ was assumed to be 0.7080; conversely, the ages are $\geq 10\%$ older if an initial $^{87}\text{Sr}/^{86}\text{Sr}$
636 value of 0.7030 is employed. **Figure 7** shows that the older the sample, the more dramatic is
637 the impact of the initial $^{87}\text{Sr}/^{86}\text{Sr}$ chosen. For the > 40 Ma Grizzas micas, the use of initial
638 $^{87}\text{Sr}/^{86}\text{Sr}$ of 0.7100 provides ages that are resolvable (i.e. outside 2SE) from those obtained
639 employing 0.7030 as the initial $^{87}\text{Sr}/^{86}\text{Sr}$ ratio. Conversely, for the younger (< 30 Ma) Megas
640 Gialos samples, all the calculated model ages are within uncertainty of each other. While the
641 favored approach remains to analyze a low Rb/Sr phase cogenetic to mica (e.g., epidote,
642 plagioclase, carbonate, apatite), where there is limited independent knowledge of initial Sr
643 isotope compositions, we recommend employing $^{87}\text{Sr}/^{86}\text{Sr}$ that are intermediate between those
644 of likely endmembers representative of the examined lithologies.

645
646 At Grizzas, the blueschist blocks (samples SYGR36 and SYGR44) and a metasomatic rind
647 (sample SYGR38) consistently yielded initial $^{87}\text{Sr}/^{86}\text{Sr}$ values close to 0.708, although the latter
648 shows scattering between 0.704 to 0.710 (**Figure 3**). In the literature, highly radiogenic values
649 in metamafic and metasomatic rocks are common in the Kampos Belt, including for some
650 metasedimentary rocks (**Figure 3**). On the other hand, a metagabbro (sample SYGR50) yielded
651 an initial $^{87}\text{Sr}/^{86}\text{Sr}$ value close to 0.705. Similarly, the metamafic greenschist (SYMG07) and
652 veins (SYMG02 and SYMG08.3), along with additional vein and greenschist samples analyzed
653 for bulk rock $^{87}\text{Sr}/^{86}\text{Sr}$ only from Megas Gialos consistently yielded in-situ epidote and age-
654 corrected TIMS whole rock $^{87}\text{Sr}/^{86}\text{Sr}$ values of ~ 0.705 (**Figure 3 and supplementary Table**
655 **S4**). We interpret the least radiogenic values to represent the oceanic magmatic protolith (e.g.,
656 Taylor and Lasaga, 1999) as well as veins that have equilibrated with or sourced from
657 metamafic rocks. In contrast, the more radiogenic signature could have been introduced by pre-
658 subduction seafloor alteration (Voigt et al., 2021), or metasomatism by highly radiogenic fluids
659 for example derived from dehydration of metasedimentary rocks (Halama et al., 2011). The
660 latter hypothesis is more consistent with the spatial association between metasedimentary and
661 metasomatic rocks within the Grizzas shear zone. Our results demonstrate that for high-
662 pressure metamafic rocks in subduction zones, the commonly assumed MORB-like $^{87}\text{Sr}/^{86}\text{Sr}$
663 value of 0.703 (Rösel and Zack, 2021) might not necessarily be representative of the initial Sr
664 isotope composition.

665



666

667 **Figure 7.** Covariation plots showing the effect of assumed initial $^{87}\text{Sr}/^{86}\text{Sr}$ on the mica Rb-Sr “model” age.
 668 Preferred anchoring values are 0.7080 ± 0.0005 for Grizzas and 0.7050 ± 0.0005 for Megas Gialos (vertical
 669 axis), which are compared to the extreme values in the range of observed bulk rock data for the Kampos Belt:
 670 0.7030 ± 0.0005 (orange) and 0.7100 ± 0.0005 (green) (horizontal axis).

671 Application to Syros

672 To further validate our newly acquired mica Rb-Sr ages (anchored to epidote or, when not
 673 available, to a modeled initial $^{87}\text{Sr}/^{86}\text{Sr}$; **Table 2**), we compare them with published age
 674 constraints from Kampos Belt (Top CBU) and Middle CBU localities (**Figure 8**). Kotowski et
 675 al. (2022) and Glodny and Ring (2022) compiled and reported new ID TIMS Rb-Sr ages,
 676 mostly from the Western Kampos Belt and outcrops along the Top CBU in Syros, ranging from
 677 53 to 43 Ma. This age range is interpreted to date the eclogite-to-blueschist-facies subduction
 678 fabrics, developed during the prograde-to-peak-pressure and earliest stage of exhumation.
 679 Robust U-Pb zircon and Lu-Hf garnet ages between 53 and 48 Ma constrain the peak
 680 metamorphism in the Grizzas area (see Tomascheck et al., 2003; Lagos et al., 2007) and are in

681 agreement with the higher end of the Rb-Sr multi-mineral isochron ages including white mica
682 separates (e.g., Glodny and Ring 2022). Recent in-situ Rb-Sr dating of white mica also showed
683 an age of 48.4 ± 3.6 Ma for an eclogite from the Kathergaki cape (presumably belonging to the
684 Top CBU), which was also interpreted to date the near-peak metamorphism (Barnes et al.,
685 2024). At Grizzas, a blueschist block (SYGR36), an altered metagabbro (SYGR42) and a
686 metasediment (SYGR45) yielded mica Rb-Sr ages varying from 46.6 ± 4.6 Ma to 47.2 ± 3.8
687 Ma (**Table 2** and **Figure 6**). Similarly, the dilational vein sample SYGR41 returned a mica Rb-
688 Sr age consistent with the HP metamorphic stage (44.7 ± 4.5 Ma). These ages overlap with the
689 low-end of the HP eclogite-to-blueschist-facies near-peak metamorphism (peak to the earliest
690 exhumation). Thus, and in line with previous investigations, the obtained ages are interpreted
691 to date near-peak metamorphism (for the blueschist SYGR36 and metasediment SYGR45
692 samples) as well as the oldest record of near-peak fluid-rock interactions and shear zone
693 development leading to veining (SYGR41) and metagabbro fluid-assisted deformation
694 (SYGR42).

695
696 Kotowski et al. (2022) and Glodny and Ring (2022) noted that ages for the retrograde stage
697 associated with early decompression in the epidote blueschist-facies are in the 45 to 40 Ma
698 range, which could also be related to a mixed signal due to partial re-equilibration between the
699 early lawsonite blueschist- and HP greenschist-facies metamorphism. Blueschist- to
700 (HP)greenschist-facies retrogression during exhumation is constrained to occur between 40 and
701 20 Ma in the Kampos Belt based on previous Rb-Sr and Ar-Ar geochronology (Glodny and
702 Ring, 2022; Kotowski et al., 2022; Laurent et al., 2017). The metasomatic rind samples
703 SYGR37 and SYGR38 yielded mica Rb-Sr ages more consistent with metasomatism and fluid-
704 rock interactions during the early exhumation stage in the epidote blueschist-facies stability
705 field (41.1 ± 3.1 Ma and 43.0 ± 5.4 Ma), although sample SYGR38 could be similarly
706 interpreted to date the metasomatism at near-peak pressure conditions considering the age
707 uncertainty. These c. 43 and 41 Ma ages date continuous fluid-rock interaction during HP
708 deformation, which preferentially occurs along shear zones (Zack and John, 2007; Angiboust
709 et al., 2014; Kleine et al., 2014; Smit and Pogge von Strandmann, 2020; Rajič et al., 2024).
710 Only one sample (felsic pod SYGR58) shows a statistically younger age of 36.1 ± 2.1 Ma,
711 which is within the period of exhumation and transition from blueschist to HP greenschist-
712 facies. This age is consistent with petrographic evidence of chlorite pseudomorphs after garnet
713 suggestive of selective greenschist-facies retrogression.

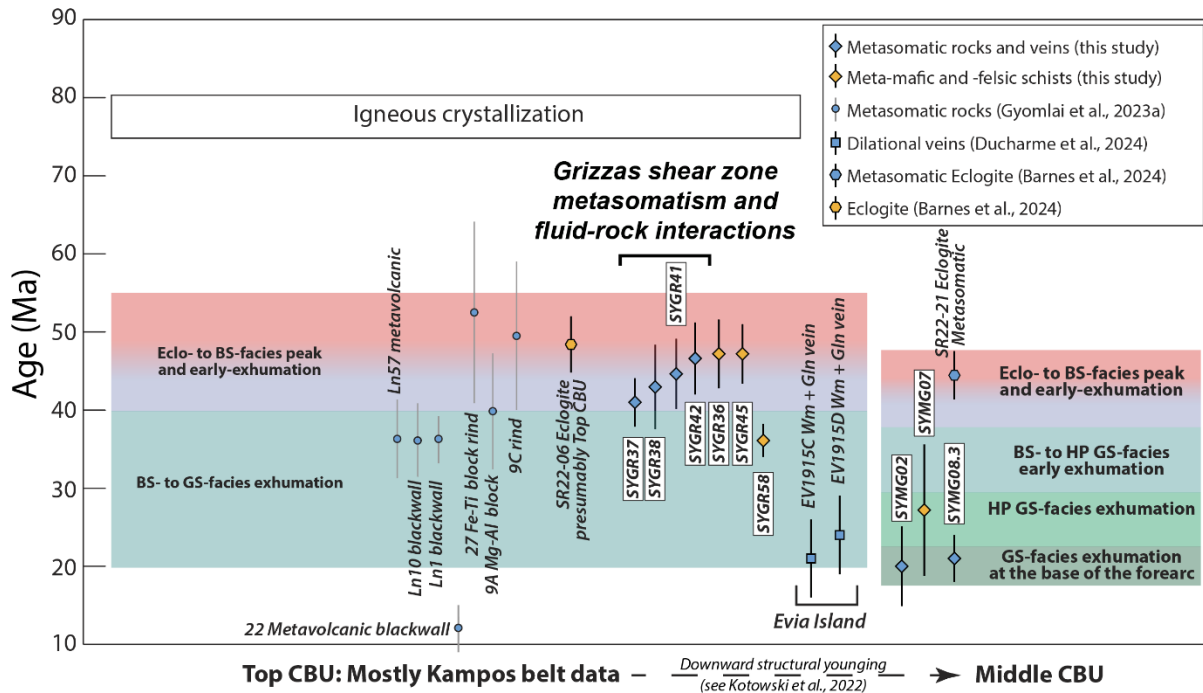
714
715 Overall, our near-peak ages align with two ages (samples 9C and 27; see **Figure 8**) reported
716 by Gyomlai et al. (2023a) for metasomatic lithologies within the Kampos Belt (Lia side), while
717 our HP early exhumation ages are comparable, within uncertainty, to one of their ages (sample
718 9A). Additionally, Gyomlai et al. (2023a) obtained three ages of c. 36 Ma (samples Ln57, Ln10
719 and Ln1), overlapping with our sample SYGR58 (felsic pod), which they interpreted as
720 retrograde ages dating the “main” metasomatic event along Kampos. Our data points to at least
721 one event of HP metasomatism and fluid-rock interactions along the Grizzas shear zone within
722 the range of 46.6 ± 4.6 Ma to 41.1 ± 3.1 Ma. Due to method uncertainties, distinguishing
723 between multiple events within this time range is not feasible. Thus, our data suggest that fluid-
724 rock interactions and metasomatism began under near-peak metamorphic conditions and

725 continued during the early stages of HP exhumation. These results agree with Ar-Ar ages
726 constraining the activity of the Lia shear zone (norther boundary of the Kampos belt; see Figure
727 1A) at near-peak to blueschist-facies exhumation conditions in the ~51 to 35 Ma range (and
728 locally down to 23 Ma due to later greenschist-facies activity; Laurent et al., 2021).
729 Furthermore, Barnes et al. (2024) reported an in-situ white mica Rb-Sr age of 44.5 ± 3.1 Ma
730 for a metasomatic eclogite (Delfini locality; presumably Middle CUB), suggesting that
731 metasomatism in this section of the nappe stack also initiated at HP conditions.

732
733 This enables us to constrain localized shear zone activity under HP conditions within the
734 subduction channel in the presence of fluids. Although previous studies have attempted to
735 estimate the P-T conditions of formation of these metasomatic lithologies along the Kampos
736 belt, the results vary widely, potentially suggesting that metasomatism may have occurred
737 throughout the prograde to exhumation path (Marschall et al., 2006; Miller et al., 2009;
738 Gyomlai et al., 2021). This is confirmed by novel reaction-path thermodynamic modelling
739 approaches, demonstrating that bulk rock compositions, particularly the activity of elements
740 such as Ca and Mg, play a primary role in the formation of these metasomatic rocks (Codillo
741 et al., 2022). These metasomatic and fluid-rock interaction events may thus be temporally and
742 spatially associated with processes such as deep slicing, underplating, and slow slip and tremor
743 (Angiboust et al., 2012; Behr et al. 2018; Agard et al., 2018; Muñoz-Montecinos et al., 2020;
744 Tewksbury-Christle et a., 2021; Behr and Bürgmann, 2021).

745
746 In the Megas Gialos locality, the host greenschist sample yielded an age of 27.4 ± 8.4 Ma, in
747 line with previous investigations of lithologies from the Middle CBU which have shown ages
748 of greenschist-facies metamorphism younger than c. 35 Ma using Ar-Ar and ID TIMS Rb-Sr
749 geochronology (Glodny and Ring, 2022; Bröcker et al., 2013). The vein samples SYMG02 and
750 SYMG08.3 yielded potentially younger (although not statistically resolvable) ages of $19.8 \pm$
751 5.2 Ma and 20.8 ± 3.1 Ma, interpreted to date dilational veining during the latest stages of
752 exhumation of the metamorphic nappe at the base of the forearc (Cisneros et al., 2020; Muñoz-
753 Montecinos and Behr, 2023). These ages align with phengite + glaucophane veins from the
754 Top CBU unit (Elvia Island), which yielded virtually identical in-situ white mica Rb-Sr
755 (anchored to glaucophane) ages for dilational veining at conditions of c. 350 °C and 0.8 GP
756 (Ducharme et al., 2024). Thus, the finding of similar ages for transitional blueschist-to-
757 greenschist-facies dilational veining in Syros and in Evia Island demonstrates that across-dip
758 fluid flow toward the forearc was an ubiquitous process that occurred along the Hellenic
759 subduction zone at c. 20-22 Ma.

760
761



762
 763 **Figure 8.** Summary of in-situ mica Rb-Sr ages from this study along with previous investigations in Syros Island
 764 and other localities along the CBU (Evia Island). The fields depicting the timing of the main tectonometamorphic
 765 events represents a synthesis of the compilations from Kotowski et al. (2022) and Glodny and Ring (2022),
 766 including white mica Rb-Sr and Ar-Ar, U-Pb in zircon and Lu-Hf in garnet, to which the reader is referred to for
 767 a more complete compilation of the geochronologic data collected in Syros and all along the CBU. BS –
 768 blueschist; Eclo – eclogite; GS – greenschist; HP – high pressure.

769 Summary

770 We systematically evaluated the limitations of mica Rb-Sr dating by LA-ICP-MS/MS for
 771 young meta-mafic samples using metamorphic rocks from Syros and attempted to circumvent
 772 these limitations by anchoring the initial $^{87}\text{Sr}/^{86}\text{Sr}$ component to either a low $^{87}\text{Rb}/^{86}\text{Sr}$ phase
 773 (i.e. epidote) or a modeled value. White mica analysis yielded narrow $^{87}\text{Rb}/^{86}\text{Sr}$ spread (ranging
 774 from 14 to 231 across the whole dataset), along with unradiogenic and imprecise $^{87}\text{Sr}/^{86}\text{Sr}$
 775 (generally <0.8 ; 2SE typically exceeding 1%). The combined effect of low $^{87}\text{Rb}/^{86}\text{Sr}$ values,
 776 limited spread in Rb/Sr and high uncertainty in $^{87}\text{Sr}/^{86}\text{Sr}$ resulted in mica-only ages (i.e. without
 777 anchoring) with very large uncertainties of 10 to 35% RSE or higher in some cases.

778
 779 By anchoring these data to a low Rb/Sr phase such as epidote, age precision improved by up
 780 to six times, aligning with previous Rb-Sr TIMS data from Syros and other localities along the
 781 Cyclades blueschists unit. Such improvement is contingent to the employment of a MC-ICP-
 782 MS instrument to obtain accurate and precise Sr isotope values for the low Rb/Sr phase by laser
 783 ablation compared to the considerably lower precision of similar analyses by LA-ICP-MS/MS
 784 (Barnes et al., 2024). A first set of samples yielded ages consistent with near-peak to early
 785 exhumation along the epidote-blueschist-facies. The youngest ages likely date the latest stage
 786 of (HP)greenschist-facies exhumation. These ages are interpreted as dating various
 787 metasomatic stages that likely initiated at near-peak metamorphic conditions and continued

788 during exhumation. We noted unexpectedly high radiogenic $^{87}\text{Sr}/^{86}\text{Sr}$ values and sometimes
789 variability for the metamafic-metasomatic materials. These values, likely resulting from
790 focused fluid flow and metasomatism along the studied shear zone, underscore the importance
791 of carefully selecting and evaluating the geologic context of $^{87}\text{Sr}/^{86}\text{Sr}$ anchors for future
792 applications of this “model” Rb-Sr white mica dating methodology.

793 **Data availability**

794 All Laser Ablation ICP-MS/MS and MC-ICP-MS data is available in the supplementary
795 material.

796 **Author contribution**

797 JM-M, AG and SV designed the study and performed the experiments, with contributions
798 from BP. JM-M and WB collected the studied samples. AG and SO developed the statistical
799 analysis. JM-M and AG prepared the manuscript with contributions from all co-authors.

800 **Competing interests**

801 The authors declare that they have no conflict of interest.

802 **Acknowledgments**

803 We would like to thank Madalina Jaggi and Marcel Guillong for invaluable technical support
804 and Heather Stoll for granting access to the Agilent 8800 employed in this work. We
805 acknowledge the constructive reviews provided by T. Gyomlai and B. Ribeiro, as well as D.
806 Rubatto for the editorial handling of this manuscript. This project was supported by the Swiss
807 National Foundation (Ambizione fellowship n. PZ00P2_180126/1 to A. Giuliani) and ERC
808 Starting Grant (947659) awarded to W.M. Behr.

809
810
811
812
813
814
815
816
817
818

References

- 820 1. Agard, P., Plunder, A., Angiboust, S., Bonnet, G., & Ruh, J. (2018). The subduction
821 plate interface: Rock record and mechanical coupling (from long to short timescales).
822 *Lithos*, 320, 537-566.
- 823 2. Angiboust, S., Wolf, S., Burov, E., Agard, P., & Yamato, P. (2012). Effect of fluid
824 circulation on subduction interface tectonic processes: Insights from thermo-
825 mechanical numerical modelling. *Earth and Planetary Science Letters*, 357, 238-248.
- 826 3. Angiboust, S., Pettke, T., De Hoog, J. C., Caron, B., & Oncken, O. (2014).
827 Channelized fluid flow and eclogite-facies metasomatism along the subduction shear
828 zone. *Journal of petrology*, 55(5), 883-916.
- 829 4. Angiboust, S., Cambeses, A., Hyppolito, T., Glodny, J., Monié, P., Calderón, M., &
830 Juliani, C. (2018). A 100-my-long window onto mass-flow processes in the
831 Patagonian Mesozoic subduction zone (Diego de Almagro Island, Chile). *Bulletin*,
832 130(9-10), 1439-1456.
- 833 5. Angiboust, S., & Glodny, J. (2020). Exhumation of eclogitic ophiolitic nappes in the
834 W. Alps: New age data and implications for crustal wedge dynamics. *Lithos*, 356,
835 105374.
- 836 6. Barnes, C. J., Zack, T., Bukala, M., Rösel, D., Mark, C., & Schneider, D. A. (2024).
837 Dating metamorphic processes and identifying $^{87}\text{Sr}/^{86}\text{Sr}$ inheritance using volume-
838 coupled Rb/Sr geochronology and geochemistry of in situ white mica: A
839 demonstration with HP/LT rocks from Syros, Greece. *Chemical Geology*, 122149.
- 840 7. Bastias, J., Spikings, R., Riley, T., Chew, D., Grunow, A., Ulianov, A., ... & Burton-
841 Johnson, A. (2023). Cretaceous magmatism in the Antarctic Peninsula and its tectonic
842 implications. *Journal of the Geological Society*, 180(1), jgs2022-067.
- 843 8. Behr, W. M., Kotowski, A. J., & Ashley, K. T. (2018). Dehydration-induced
844 rheological heterogeneity and the deep tremor source in warm subduction zones.
845 *Geology*, 46(5), 475-478.
- 846 9. Behr, W. M., & Bürgmann, R. (2021). What's down there? The structures, materials
847 and environment of deep-seated slow slip and tremor. *Philosophical Transactions of*
848 *the Royal Society A*, 379(2193), 20200218.
- 849 10. v. Blanckenburg, F., Villa, I. M., Baur, H., Morteani, G., & Steiger, R. H. (1989).
850 Time calibration of a PT-path from the Western Tauern Window, Eastern Alps: the
851 problem of closure temperatures. *Contributions to mineralogy and Petrology*, 101(1),
852 1-11.
- 853 11. Breeding, C. M., Ague, J. J., & Bröcker, M. (2004). Fluid–metasedimentary rock
854 interactions in subduction-zone mélangé: implications for the chemical composition
855 of arc magmas. *Geology*, 32(12), 1041-1044.
- 856 12. Bröcker, M., & Enders, M. (2001). Unusual bulk-rock compositions in eclogite-facies
857 rocks from Syros and Tinos (Cyclades, Greece): implications for U–Pb zircon
858 geochronology. *Chemical Geology*, 175(3-4), 581-603.
- 859 13. Bröcker, M., Baldwin, S., & Arkudas, R. (2013). The geological significance of
860 $^{40}\text{Ar}/^{39}\text{Ar}$ and Rb–Sr white mica ages from Syros and Sifnos, Greece: a record of
861 continuous (re) crystallization during exhumation?. *Journal of Metamorphic Geology*,
862 31(6), 629-646.

- 863 14. Burg, J. P., & Bouilhol, P. (2019). Timeline of the South Tibet–Himalayan belt: The
864 geochronological record of subduction, collision, and underthrusting from zircon and
865 monazite U–Pb ages. *Canadian Journal of Earth Sciences*, 56(12), 1318-1332.
- 866 15. Ceccato, A., Behr, W. M., Zappone, A. S., Tavazzani, L., & Giuliani, A. (2024).
867 Structural evolution, exhumation rates, and rheology of the European crust during
868 Alpine collision: Constraints from the Rotondo granite—Gotthard nappe. *Tectonics*,
869 43, e2023TC008219.
- 870 16. Chew, D. M., & Spikings, R. A. (2015). Geochronology and thermochronology using
871 apatite: time and temperature, lower crust to surface. *Elements*, 11(3), 189-194.
- 872 17. Cisneros, M., Barnes, J. D., Behr, W. M., Kotowski, A. J., Stockli, D. F., & Soukis,
873 K. (2020). Insights from elastic thermobarometry into exhumation of high-pressure
874 metamorphic rocks from Syros, Greece. *Solid Earth Discussions*, 2020, 1-27.
- 875 18. Cooperdock, E. H., Raia, N. H., Barnes, J. D., Stockli, D. F., & Schwarzenbach, E. M.
876 (2018). Tectonic origin of serpentinites on Syros, Greece: Geochemical signatures of
877 abyssal origin preserved in a HP/LT subduction complex. *Lithos*, 296, 352-364.
- 878 19. Dalton, H., Giuliani, A., Phillips, D., Hergt, J., Maas, R., Matchan, E., ... & O'Brien,
879 H. (2020). A comparison of geochronological methods commonly applied to
880 kimberlites and related rocks: Three case studies from Finland. *Chemical Geology*,
881 558, 119899.
- 882 20. Ducharme, T. A., Schneider, D. A., Grasemann, B., Bukala, M., Camacho, A.,
883 Larson, K. P., & Soukis, K. (2024). Syn-exhumation metasomatic glaucophane-
884 phengite-quartz veins formed at moderate pressures: exploring the control of fO₂ and
885 bulk composition on nominally HP metamorphic assemblages. *Contributions to
886 Mineralogy and Petrology*, 179(3), 1-25.
- 887 21. Fitzpayne, A., Giuliani, A., Hergt, J., Woodhead, J. D., & Maas, R. (2020). Isotopic
888 analyses of clinopyroxenes demonstrate the effects of kimberlite melt metasomatism
889 upon the lithospheric mantle. *Lithos*, 370, 105595.
- 890 22. Fitzpayne, A., Giuliani, A., Howarth, G. H., Peters, B. J., Fehr, M. A., & Maas, R.
891 (2023). Major-, trace-element and Sr-Nd-Hf isotope geochemistry of diamondiferous
892 dykes from Tonguma and Koidu, Sierra Leone: highly micaceous kimberlites formed
893 by assimilation of metasomatised lithospheric mantle rocks. *Chemical Geology*, 630,
894 121475.
- 895 23. Gautier, P., & Brun, J. P. (1994). Ductile crust exhumation and extensional
896 detachments in the central Aegean (Cyclades and Evvia Islands). *Geodinamica Acta*,
897 7(2), 57-85.
- 898 24. Giuliani, A., Oesch, S., Guillong, M., & Howarth, G. H. (2024). Mica RbSr dating by
899 laser ablation ICP-MS/MS using an isochronous calibration material and application
900 to West African kimberlites. *Chemical Geology*, 121982.
- 901 25. Glodny, J., Grauert, B., Fiala, J., Vejnar, Z., & Krohe, A. (1998). Metapegmatites in
902 the western Bohemian massif: ages of crystallisation and metamorphic overprint, as
903 constrained by U–Pb zircon, monazite, garnet, columbite and Rb–Sr muscovite data.
904 *Geologische Rundschau*, 87, 124-134.
- 905 26. Glodny, J., Pease, V., Montero, P., Austrheim, H., & Rusin, A. I. (2004). Protolith
906 ages of eclogites, Marun-Keu Complex, Polar Urals, Russia: implications for the pre-
907 and early Uralian evolution of the northeastern European continental margin.
908 *Geological Society, London, Memoirs*, 30(1), 87-105.
- 909 27. Glodny, J., Kühn, A., & Austrheim, H. (2008). Geochronology of fluid-induced
910 eclogite and amphibolite facies metamorphic reactions in a subduction–collision
911 system, Bergen Arcs, Norway. *Contributions to Mineralogy and Petrology*, 156, 27-
912 48.

- 913 28. Glodny, J., & Ring, U. (2022). The Cycladic Blueschist Unit of the Hellenic
914 subduction orogen: Protracted high-pressure metamorphism, decompression and
915 reimbrication of a diachronous nappe stack. *Earth-Science Reviews*, 224, 103883.
- 916 29. Gou, L. L., Long, X. P., Yan, H. Y., Shu, T. C., Wang, J. Y., Xu, X. F., ... & Tian, Z.
917 B. (2022). Metamorphic P–T Evolution and In Situ Biotite Rb–Sr Geochronology of
918 Garnet–Staurolite Schist From the Ramba Gneiss Dome in the Northern Himalaya.
919 *Frontiers in Earth Science*, 10, 887154.
- 920 30. Gyomlai, T., Agard, P., Jolivet, L., Larvet, T., Bonnet, G., Omrani, J., ... & Noël, J.
921 (2022). Cimmerian metamorphism and post Mid-Cimmerian exhumation in Central
922 Iran: Insights from in-situ Rb/Sr and U/Pb dating. *Journal of Asian Earth Sciences*,
923 233, 105242.
- 924 31. Gyomlai, T., Agard, P., Marschall, H. R., & Jolivet, L. (2023a). Hygrochronometry of
925 punctuated metasomatic events during exhumation of the Cycladic blueschist unit
926 (Syros, Greece). *Terra Nova*, 35(2), 101-112.
- 927 32. Gyomlai, T., Agard, P., Herviou, C., Jolivet, L., Monié, P., Mendes, K., & Iemmolo,
928 A. (2023b). In situ Rb–Sr and ⁴⁰Ar–³⁹Ar dating of distinct mica generations in the
929 exhumed subduction complex of the Western Alps. *Contributions to Mineralogy and
930 Petrology*, 178(9), 58.
- 931 33. Halama, R., John, T., Herms, P., Hauff, F., & Schenk, V. (2011). A stable (Li, O) and
932 radiogenic (Sr, Nd) isotope perspective on metasomatic processes in a subducting
933 slab. *Chemical Geology*, 281(3-4), 151-166.
- 934 34. Halama, R., Konrad-Schmolke, M., & De Hoog, J. C. (2020). Boron isotope record of
935 peak metamorphic ultrahigh-pressure and retrograde fluid–rock interaction in white
936 mica (Lago di Cignana, Western Alps). *Contributions to Mineralogy and Petrology*,
937 175(3), 20.
- 938 35. Hogmalm, K.J., Zack, T., Karlsson, A.K.O., Sjöqvist, A.S.L., Garbe-Schönberg, D.,
939 2017. In situ Rb–Sr and K–Ca dating by LA-ICP-MS/MS: an evaluation of N₂O and
940 SF₆ as reaction gases. *Journal of Analytical Atomic Spectrometry* 32(2), 305-313.
- 941 36. Holtmann, R., Muñoz-Montecinos, J., Angiboust, S., Cambeses, A., Bonnet, G.,
942 Brown, A., ... & Agard, P. (2022). Cretaceous thermal evolution of the closing Neo-
943 Tethyan realm revealed by multi-method petrochronology. *Lithos*, 422, 106731.
- 944 37. Huang, C., Wang, H., Shi, W., Sun, J., Hu, F., Xu, L., ... & Yang, J. (2023). In situ
945 Rb-Sr dating of mica by LA-ICP-MS/MS. *Science China Earth Sciences*, 66(11),
946 2603-2621.
- 947 38. Hyppolito, T., Angiboust, S., Juliani, C., Glodny, J., Garcia-Casco, A., Calderón, M.,
948 & Chopin, C. (2016). Eclogite-, amphibolite- and blueschist-facies rocks from Diego
949 de Almagro Island (Patagonia): Episodic accretion and thermal evolution of the
950 Chilean subduction interface during the Cretaceous. *Lithos*, 264, 422-440.
- 951 39. Jäger, E., Niggli, E., Wenk, E., 1967. Rb-Sr Altersbestimmungen an Glimmern der
952 Zentralalpen. In: *Beiträge zur Geologischen Karte der Schweiz*. vol. 134 Kümmerly &
953 Frey, Bern.
- 954 40. John, T., Gussone, N., Podladchikov, Y. Y., Bebout, G. E., Dohmen, R., Halama, R.,
955 ... & Seitz, H. M. (2012). Volcanic arcs fed by rapid pulsed fluid flow through
956 subducting slabs. *Nature Geoscience*, 5(7), 489-492.
- 957 41. Jolivet, L., Lecomte, E., Huet, B., Denèle, Y., Lacombe, O., Labrousse, L., ... & Mehl,
958 C. (2010). The north cycladic detachment system. *Earth and Planetary Science
959 Letters*, 289(1-2), 87-104.
- 960 42. Keay, S., 1998. The Geological Evolution of the Cyclades, Greece: Constraints from
961 SHRIMP U-Pb Geochronology. Unpublished PhD Thesis . Australian National
962 University , Canberra .

- 963 43. Keiter, M., Ballhaus, C., & Tomaschek, F. (2011). A new geological map of the
964 Island of Syros (Aegean Sea, Greece): Implications for lithostratigraphy and structural
965 history of the Cycladic Blueschist Unit (Vol. 481). Geological Society of America.
966 44. Kirchner, K. L., Behr, W. M., Loewy, S., & Stockli, D. F. (2016). Early Miocene
967 subduction in the western Mediterranean: Constraints from Rb-Sr multiminerall
968 isochron geochronology. *Geochemistry, Geophysics, Geosystems*, 17(5), 1842-1860.
969 45. Kirkland, C. L., Olierook, H. K., Danišik, M., Liebmann, J., Hollis, J., Ribeiro, B. V.,
970 & Rankenburg, K. (2023). Dating mylonitic overprinting of ancient rocks.
971 *Communications Earth & Environment*, 4(1), 47.
972 46. Kleine, B. I., Skelton, A. D., Huet, B., & Pitcairn, I. K. (2014). Preservation of
973 blueschist-facies minerals along a shear zone by coupled metasomatism and fast-
974 flowing CO₂-bearing fluids. *Journal of Petrology*, 55(10), 1905-1939.
975 47. Kotowski, A. J., Cisneros, M., Behr, W. M., Stockli, D. F., Soukis, K., Barnes, J. D.,
976 & Ortega-Arroyo, D. (2022). Subduction, underplating, and return flow recorded in
977 the Cycladic Blueschist Unit exposed on Syros, Greece. *Tectonics*, 41(6),
978 e2020TC006528.
979 48. Kutzschbach, M., & Glodny, J. (2024). LA-ICP-MS/MS-based Rb–Sr isotope
980 mapping for geochronology. *Journal of Analytical Atomic Spectrometry*, 39(2), 455-
981 477.
982 49. Lagos, M., Scherer, E. E., Tomaschek, F., Münker, C., Keiter, M., Berndt, J., &
983 Ballhaus, C. (2007). High precision Lu–Hf geochronology of Eocene eclogite-facies
984 rocks from Syros, Cyclades, Greece. *Chemical Geology*, 243(1-2), 16-35.
985 50. Laurent, V., Lanari, P., Nair, I., Augier, R., Lahfid, A., & Jolivet, L. (2018).
986 Exhumation of eclogite and blueschist (Cyclades, Greece): Pressure–temperature
987 evolution determined by thermobarometry and garnet equilibrium modelling. *Journal*
988 *of metamorphic geology*, 36(6), 769-798.
989 51. Li, K., Li, G. Y., Du, Y. F., Han, W., Zhang, J., Chen, L. H., ... & Li, L. (2021).
990 Intraslab remobilization of nitrogen during early subduction facilitates deep nitrogen
991 recycling: Insights from the blueschists in the Heilongjiang Complex in NE China.
992 *Chemical Geology*, 583, 120474.
993 52. Marschall, H. R., Ludwig, T., Altherr, R., Kalt, A., & Tonarini, S. (2006). Syros
994 metasomatic tourmaline: evidence for very high- $\delta^{11}\text{B}$ fluids in subduction zones.
995 *Journal of Petrology*, 47(10), 1915-1942.
996 53. Miller, D. P., Marschall, H. R., & Schumacher, J. C. (2009). Metasomatic formation
997 and petrology of blueschist-facies hybrid rocks from Syros (Greece): Implications for
998 reactions at the slab–mantle interface. *Lithos*, 107(1-2), 53-67.
999 54. Muñoz-Montecinos, J., Angiboust, S., Cambeses, A., & García-Casco, A. (2020).
1000 Multiple veining in a paleo–accretionary wedge: The metamorphic rock record of
1001 prograde dehydration and transient high pore-fluid pressures along the subduction
1002 interface (Western Series, central Chile). *Geosphere*, 16(3), 765-786.
1003 55. Muñoz-Montecinos, J., Angiboust, S., & Garcia-Casco, A. (2021). Blueschist-facies
1004 paleo-earthquakes in a serpentinite channel (Zagros suture, Iran) enlighten
1005 seismogenesis in Mariana-type subduction margins. *Earth and Planetary Science*
1006 *Letters*, 573, 117135.
1007 56. Muñoz-Montecinos, J., & Behr, W. M. (2023). Transient Permeability of a Deep-
1008 Seated Subduction Interface Shear Zone. *Geophysical Research Letters*, 50(20),
1009 e2023GL104244.
1010 57. Olierook, H. K., Rankenburg, K., Ulrich, S., Kirkland, C. L., Evans, N., Brown, S., ...
1011 & Darragh, M. (2020). Resolving multiple geological events using in situ Rb-Sr

- 1012 geochronology: implications for metallogensis at Tropicana, Western Australia.
1013 Geochronology Discussions, 2020, 1-31.
- 1014 58. Paton, C., Woodhead, J. D., Hergt, J. M., Phillips, D., & Shee, S. (2007). Strontium
1015 isotope analysis of kimberlitic groundmass perovskite via LA-MC-ICP-MS.
1016 Geostandards and Geoanalytical Research, 31(4), 321-330.
- 1017 59. Paton, C., Hellstrom, J., Paul, B., Woodhead, J., & Hergt, J. (2011). Iolite: Freeware
1018 for the visualisation and processing of mass spectrometric data. Journal of Analytical
1019 Atomic Spectrometry, 26(12), 2508-2518.
- 1020 60. Phillips, D., Zhong, D., Matchan, E. L., Maas, R., Farr, H., O'Brien, H., & Giuliani,
1021 A. (2017, September). A comparison of geochronology methods applied to
1022 kimberlites and related rocks from the Karelian Craton, Finland. In International
1023 Kimberlite Conference: Extended Abstracts (Vol. 11).
- 1024 61. Pimenta Silva, M., Marxer, F., Keller, T., Giuliani, A., Ulmer, P., & Müntener, O.
1025 (2023). Alkaline magmas in shallow arc plutonic roots: a field and experimental
1026 investigation of hydrous cumulate melting in the southern Adamello batholith.
1027 Contributions to Mineralogy and Petrology, 178(9), 64.
- 1028 62. Plank, T. (2014). The chemical composition of subducting sediments. Elsevier.
- 1029 63. Putlitz, B., Cosca, M. A., & Schumacher, J. C. (2005). Prograde mica $40\text{Ar}/39\text{Ar}$
1030 growth ages recorded in high pressure rocks (Syros, Cyclades, Greece). Chemical
1031 Geology, 214(1-2), 79-98.
- 1032 64. Redaa, A., Farkaš, J., Gilbert, S., Collins, A. S., Wade, B., Löhr, S., ... & Garbe-
1033 Schönberg, D. (2021). Assessment of elemental fractionation and matrix effects
1034 during in situ Rb–Sr dating of phlogopite by LA-ICP-MS/MS: implications for the
1035 accuracy and precision of mineral ages. Journal of Analytical Atomic Spectrometry,
1036 36(2), 322-344.
- 1037 65. Regis, D., Rubatto, D., Darling, J., Cenki-Tok, B., Zucali, M., & Engi, M. (2014).
1038 Multiple metamorphic stages within an eclogite-facies terrane (Sesia Zone, Western
1039 Alps) revealed by Th–U–Pb petrochronology. Journal of Petrology, 55(7), 1429-1456.
- 1040 66. Ribeiro, B. V., Finch, M. A., Cawood, P. A., Faleiros, F. M., Murphy, T. D.,
1041 Simpson, A., ... & Barrote, V. R. (2022). From microanalysis to supercontinents:
1042 insights from the Rio Apa Terrane into the Mesoproterozoic SW Amazonian Craton
1043 evolution during Rodinia assembly. Journal of Metamorphic Geology, 40(4), 631-
1044 663.
- 1045 67. Ribeiro, B. V., Kirkland, C. L., Kelsey, D. E., Reddy, S. M., Hartnady, M. I., Faleiros,
1046 F. M., ... & Clark, C. (2023a). Time-strain evolution of shear zones from
1047 petrographically constrained Rb–Sr muscovite analysis. Earth and Planetary Science
1048 Letters, 602, 117969.
- 1049 68. Ribeiro, B. V., Kirkland, C. L., Finch, M. A., Faleiros, F. M., Reddy, S. M., Rickard,
1050 W. D., & Michael, I. H. (2023b). Microstructures, geochemistry, and geochronology
1051 of mica fish: Review and advances. Journal of Structural Geology, 104947.
- 1052 69. Rubatto, D., Regis, D., Hermann, J., Boston, K., Engi, M., Beltrando, M., &
1053 McAlpine, S. R. (2011). Yo-yo subduction recorded by accessory minerals in the
1054 Italian Western Alps. Nature Geoscience, 4(5), 338-342.
- 1055 70. Rubatto, D., Williams, M., Markmann, T. A., Hermann, J., & Lanari, P. (2023).
1056 Tracing fluid infiltration into oceanic crust up to ultra-high-pressure conditions.
1057 Contributions to Mineralogy and Petrology, 178(11), 79.
- 1058 71. Salters, V. J., & Stracke, A. (2004). Composition of the depleted mantle.
1059 Geochemistry, Geophysics, Geosystems, 5(5).
- 1060 72. Sarkar, S., Giuliani, A., Dalton, H., Phillips, D., Ghosh, S., Misev, S., & Maas, R.
1061 (2023). Derivation of Lamproites and Kimberlites from a Common Evolving Source

- 1062 in the Convective Mantle: the Case for Southern African ‘Transitional Kimberlites’.
1063 *Journal of Petrology*, 64(7), egad043.
- 1064 73. Schmidt, M. W., Vielzeuf, D., & Auzanneau, E. (2004). Melting and dissolution of
1065 subducting crust at high pressures: the key role of white mica. *Earth and Planetary
1066 Science Letters*, 228(1-2), 65-84.
- 1067 74. Seman, S., Stockli, D. F., & Soukis, K. (2017). The provenance and internal structure
1068 of the Cycladic Blueschist Unit revealed by detrital zircon geochronology, Western
1069 Cyclades, Greece. *Tectonics*, 36(7), 1407-1429.
- 1070 75. Smit, M. A., & von Strandmann, P. A. P. (2020). Deep fluid release in warm
1071 subduction zones from a breached slab seal. *Earth and Planetary Science Letters*, 534,
1072 116046.
- 1073 76. Soukis, K., & Stockli, D. F. (2013). Structural and thermochronometric evidence for
1074 multi-stage exhumation of southern Syros, Cycladic islands, Greece. *Tectonophysics*,
1075 595, 148-164.
- 1076 77. Tewksbury-Christle, C. M., Behr, W. M., & Helper, M. A. (2021). Tracking deep
1077 sediment underplating in a fossil subduction margin: Implications for interface
1078 rheology and mass and volatile recycling. *Geochemistry, Geophysics, Geosystems*,
1079 22(3), e2020GC009463.
- 1080 78. Tillberg, M., Drake, H., Zack, T., Kooijman, E., Whitehouse, M. J., & Åström, M. E.
1081 (2020). In situ Rb-Sr dating of slickenfibres in deep crystalline basement faults.
1082 *Scientific reports*, 10(1), 562.
- 1083 79. Tillberg, M., Drake, H., Zack, T., Hogmalm, J., Kooijman, E., & Åström, M. (2021).
1084 Reconstructing craton-scale tectonic events via in situ Rb-Sr geochronology of poly-
1085 phased vein mineralization. *Terra Nova*, 33(5), 502-510.
- 1086 80. Tomaschek, F., Kennedy, A. K., Villa, I. M., Lagos, M., & Ballhaus, C. (2003).
1087 Zircons from Syros, Cyclades, Greece—recrystallization and mobilization of zircon
1088 during high-pressure metamorphism. *Journal of Petrology*, 44(11), 1977-2002.
- 1089 81. Trotet, F., Jolivet, L., & Vidal, O. (2001). Tectono-metamorphic evolution of Syros
1090 and Sifnos islands (Cyclades, Greece). *Tectonophysics*, 338(2), 179-206.
- 1091 82. Rajič, K., Raimbourg, H., Gion, A. M., Lerouge, C., & Erdmann, S. (2024). Tracing
1092 the Scale of Fluid Flow in Subduction Zone Forearcs: Implications from Fluid-Mobile
1093 elements. *Chemical Geology*, 122141.
- 1094 83. Redaa, A., Farkaš, J., Hassan, A., Collins, A. S., Gilbert, S., & Löhr, S. C. (2022).
1095 Constraints from in-situ Rb-Sr dating on the timing of tectono-thermal events in the
1096 Umm Farwah shear zone and associated Cu-Au mineralisation in the Southern
1097 Arabian Shield, Saudi Arabia. *Journal of Asian Earth Sciences*, 224, 105037.
- 1098 84. Taylor, A. S., & Lasaga, A. C. (1999). The role of basalt weathering in the Sr isotope
1099 budget of the oceans. *Chemical Geology*, 161(1-3), 199-214.
- 1100 85. Zack, T., & Roesel, D. (2021, December). Towards robust in-situ Rb-Sr spot ages. In
1101 AGU Fall Meeting Abstracts (Vol. 2021, pp. V22A-04).
- 1102 86. Uunk, B., Brouwer, F., ter Voorde, M., & Wijbrans, J. (2018). Understanding
1103 phengite argon closure using single grain fusion age distributions in the Cycladic
1104 Blueschist Unit on Syros, Greece. *Earth and Planetary Science Letters*, 484, 192-203.
- 1105 87. Vermeesch, P. (2018). IsoplotR: A free and open toolbox for geochronology.
1106 *Geoscience Frontiers*, 9(5), 1479-1493.
- 1107 88. Villa. (1998). Isotopic closure. *Terra nova*, 10(1), 42-47.
- 1108 89. Villa, I. M. (2016). Diffusion in mineral geochronometers: Present and absent.
1109 *Chemical Geology*, 420, 1-10.

- 1110 90. Villa, I.M., De Bièvre, P., Holden, N.E., Renne, P.R., 2015. IUPAC-IUGS
1111 recommendation on the half life of ^{87}Rb . *Geochimica et Cosmochimica Acta* 164,
1112 382-385.
- 1113 91. Voigt, M., Pearce, C. R., Baldermann, A., & Oelkers, E. H. (2018). Stable and
1114 radiogenic strontium isotope fractionation during hydrothermal seawater-basalt
1115 interaction. *Geochimica et Cosmochimica Acta*, 240, 131-151.
- 1116 92. Volante, S., Blereau, E., Guitreau, M., Tedeschi, M., van Schijndel, V., & Cutts, K.
1117 (2024). Current applications using key mineral phases in igneous and metamorphic
1118 geology: perspectives for the future. Geological Society, London, Special
1119 Publications, 537(1), 57-121.
- 1120 93. Wang, C., Alard, O., Lai, Y. J., Foley, S. F., Liu, Y., Munnikhuis, J., & Wang, Y.
1121 (2022). Advances in in-situ Rb-Sr dating using LA-ICP-MS/MS: applications to
1122 igneous rocks of all ages and to the identification of unrecognized metamorphic
1123 events. *Chemical Geology*, 610, 121073.
- 1124 94. Wawrzenitz, N., Romer, R. L., Oberhänsli, R., & Dong, S. (2006). Dating of
1125 subduction and differential exhumation of UHP rocks from the Central Dabie
1126 Complex (E-China): constraints from microfabrics, Rb–Sr and U–Pb isotope systems.
1127 *Lithos*, 89(1-2), 174-201.
- 1128 95. Whitney, D. L., & Evans, B. W. (2010). Abbreviations for names of rock-forming
1129 minerals. *American mineralogist*, 95(1), 185-187.
- 1130 96. Wirth, E. A., Sahakian, V. J., Wallace, L. M., & Melnick, D. (2022). The occurrence
1131 and hazards of great subduction zone earthquakes. *Nature Reviews Earth &*
1132 *Environment*, 3(2), 125-140.
- 1133 97. Zack, T., Hogmalm, K.J., 2016. Laser ablation Rb/Sr dating by online chemical
1134 separation of Rb and Sr in an oxygen-filled reaction cell. *Chemical Geology* 437, 120-
1135 133.
- 1136 98. Zack, T., & John, T. (2007). An evaluation of reactive fluid flow and trace element
1137 mobility in subducting slabs. *Chemical Geology*, 239(3-4), 199-216.
- 1138 99. Zametzer, A., Kirkland, C. L., Barham, M., Hartnady, M. I., Bath, A. B., &
1139 Rankenburg, K. (2022). Episodic alteration within a gold-bearing Archean shear zone
1140 revealed by in situ biotite Rb–Sr dating. *Precambrian Research*, 382, 106872.
- 1141 100. Zhao, H., Zhao, X. M., Le Roux, P. J., Zhang, W., Wang, H., Xie, L. W., ... &
1142 Yang, Y. H. (2020). Natural clinopyroxene reference materials for in situ Sr isotopic
1143 analysis via LA-MC-ICP-MS. *Frontiers in Chemistry*, 8, 594316.
- 1144